The XXL Survey: third series

Astronomy & Astrophysics

Special issue

The XXL Survey

XL. Obscuration properties of red AGNs in XXL-N

V. A. Masoura[1,2], I. Georgantopoulos[1], G. Mountrichas[3,1], C. Vignali[4,5], E. Koulouridis[1,6], L. Chiappetti[7],
S. Fotopoulou[8], S. Paltani[9], and M. Pierre[6]

[1] National Observatory of Athens, V. Paulou & I. Metaxa, 15 236 Penteli, Greece
e-mail: `vmasoura@noa.gr`
[2] Section of Astrophysics, Astronomy and Mechanics, Department of Physics, Aristotle University of Thessaloniki,
54 124 Thessaloniki, Greece
[3] Instituto de Fisica de Cantabria (CSIC-Universidad de Cantabria), Avenida de los Castros, 39005 Santander, Spain
[4] Dipartimento di Fisica e Astronomia, Alma Mater Studiorum, Universitá degli Studi di Bologna, Via Gobetti 93/2, 40129 Bologna,
Italy
[5] INAF – Osservatorio di Astrofisica e Scienza dello Spazio di Bologna, Via Gobetti 93/3, 40129 Bologna, Italy
[6] AIM, CEA, CNRS, Université Paris-Saclay, Université Paris Diderot, Sorbonne Paris Cité, 91191 Gif-sur-Yvette, France
[7] INAF, IASF Milano, Via Corti 12, 20133 Milano, Italy
[8] Centre for Extragalactic Astronomy, Department of Physics, Durham University, Durham DH1 3LE, UK
[9] Department of Astronomy, University of Geneva, Ch. d'Écogia 16, 1290 Versoix, Switzerland

ABSTRACT

The combination of optical and mid-infrared (MIR) photometry has been extensively used to select red active galactic nuclei (AGNs). Our aim is to explore the obscuration properties of these red AGNs with both X-ray spectroscopy and spectral energy distributions (SEDs). In this study, we re-visit the relation between optical/MIR extinction and X-ray absorption. We use IR selection criteria, specifically the $W1$ and $W2$ WISE bands, to identify 4798 AGNs in the XMM-XXL area ($\sim$25 deg^2). Application of optical/MIR colours ($r-W2 > 6$) reveals 561 red AGNs (14%). Of these, 47 have available X-ray spectra with at least 50 net (background-subtracted) counts per detector. For these sources, we construct SEDs from the optical to the MIR using the CIGALE code. The SED fitting shows that 44 of these latter 47 sources present clear signs of obscuration based on the AGN emission and the estimated inclination angle. Fitting the SED also reveals ten systems ($\sim$20%) which are dominated by the galaxy. In these cases, the red colours are attributed to the host galaxy rather than AGN absorption. Excluding these ten systems from our sample and applying X-ray spectral fitting analysis shows that up to 76% (28/37) of the IR red AGNs present signs of X-ray absorption. Thus, there are nine sources ($\sim$20% of the sample) that although optically red, are not substantially X-ray absorbed. Approximately 50% of these sources present broad emission lines in their optical spectra. We suggest that the reason for this apparent discrepancy is that the $r-W2$ criterion is sensitive to smaller amounts of obscuration relative to the X-ray spectroscopy. In conclusion, it appears that the majority of red AGNs present considerable obscuration levels as shown by their SEDs. Their X-ray absorption is moderate with a mean of $N_{\rm H} \sim 10^{22}$ cm^{-2}.

Key words. galaxies: active – X-rays: galaxies

1. Introduction

The vast majority of galaxies host a supermassive black hole (SMBH) in their centre (e.g. Kormendy et al. 1996a,b). The masses of these SMBHs range from hundreds of thousands to billions of solar masses ($\approx 10^5-10^{10}\ M_\odot$). When a SMBH grows, it releases huge amounts of energy across the electromagnetic spectrum and becomes visible as an AGN. These latter objects have characteristic properties such as high luminosities (up to $L_{\rm bol} \simeq 10^{48}$ erg s^{-1}) and rapid variability (e.g. Ulrich et al. 1997).

According to the unification scheme (Antonucci 1993) the central source of the AGN structure consists of the SMBH, the corona, and the accretion disc. These regions are surrounded by an axisymmetric dusty structure that is toroidal in shape (e.g. Netzer 2015). Starting from the inner part of the source, the X-ray and the optical/ultraviolet (UV) wavelengths are related to the corona and the accretion disc respectively (e.g. Wilkins & Gallo 2015; Haardt & Maraschi 1991). The torus is responsible for the infrared (IR) emission (e.g.

Edelson & Malkan 1986), because the hot dust is related to the radiation at these wavelengths. There are different torus models based on the distribution of dust, such as smooth (e.g. Fritz et al. 2006), clumpy (Nenkova et al. 2008a,b; Hönig & Kishimoto 2010, 2017; Hönig et al. 2010), and a combination of the two (Siebenmorgen et al. 2015; Stalevski et al. 2016). Unified models propose that the different observational classes of AGNs are nevertheless a single type of physical object observed at different viewing angles (e.g. different orientations of the observer with respect to the torus). Thus, Type 1 and Type 2 AGNs refer to the face-on (unobscured) and edge-on (obscured) AGNs, respectively. However, in the case of a clumpy torus, the classification of AGN type is not necessarily a consequence of a difference in viewing angle, because the dust is not distributed homogeneously. Based on their optical/UV spectrum, Type 1 AGNs present broad permitted emission lines, while Type 2 objects show only narrow lines. There is a continuum of objects in between (intermediate types), where the broad line components are increasingly difficult to observe.

Table 1. Number of IR-selected AGNs with X-ray and optical observations and spectra in the XMM-XXL field.

	Total number	X-ray detections	X-ray spectra
IR AGNs	4798	1503	312
IR AGNs with SDSS	2652	1268	262
Red AGNs	561	135	47

Despite the huge radiative power of AGNs, obscuration presents an important challenge for uncovering their complete population and explaining the complicated mechanisms that regulate these systems (Hickox & Alexander 2018). Regarding the different obscuring material, X-ray energies are obscured by gas, whereas UV, optical, and IR wavelengths are extincted by dust. A reliable method to identify and quantify obscuration is through X-ray observations. Modelling of the X-ray spectrum provides a robust estimation of the N_H column density.

The combination of optical and IR data also provides us with a powerful tool to search for obscured AGNs. The optical emission of a SMBH is attenuated by dust and is re-emitted in the NIR to MIR wavelengths. In this case the galaxy appears faint in the optical but bright in the IR (LaMassa et al. 2016). Various optical and IR colour criteria have been used in the literature to identify red AGNs, using either *Spitzer* (e.g. Fiore et al. 2009; Hickox et al. 2007; LaMassa et al. 2016; Donoso et al. 2014) or WISE (Yan et al. 2013) IR bands.

Previous studies have found a correlation between the optical/IR colours and X-ray absorption (e.g. Civano et al. 2012). On the other hand, Koutoulidis et al. (2018) found that reddened AGNs are equally divided into X-ray absorbed and unabsorbed. Specifically, these latter authors used about 1500 X-ray AGNs from five deep *Chandra* fields (CDF-N, CDF-S, ECDF-S, COSMOS, AEGIS) and divided them into obscured and unobscured sources using X-ray (Hardness Ratio) and optical/midinfrared (MIR) criteria ($R - [4.5] = 6.1$). Nevertheless their sources span low luminosities (10^{42}–10^{43} erg s^{-1}). Based on their findings Koutoulidis et al. suggested that host galaxy contamination in the MIR bands affects the optical/MIR AGN classification.

We examine whether or not red AGNs are also absorbed in X-rays. To this aim, we use X-ray AGNs in the XXL survey (Pierre et al. 2016, hereafter XXL paper I) and select IR AGN candidates by applying the criteria of Assef et al. (2018). We use optical and MIR colours (Yan et al. 2013) to select optically red sources. The final sample is restricted to those AGNs for which X-ray spectroscopy is available (47 sources). In Sect. 3.1 we fit the X-ray spectra to quantify the X-ray absorption of the sources. In addition we construct spectral energy distributions (SEDs) using optical, near-infrared (NIR), and MIR photometry. We use the CIGALE code (Ciesla et al. 2015) to fit the SEDs and get an estimation of various absorption indices (AGN emission, torus inclination). We also complement our analysis with available optical spectra (see Sect. 3.3). Finally, we compare the results of different wavelengths and techniques for each red AGN.

2. Data

The data of this study come from the XXL survey. In this section we describe the survey as well as the sample selection.

2.1. XXL

The XXL survey is a medium-depth X-ray survey that covers a total area of 50 deg^2. It covers two fields of nearly equal size, the XXL North (XXL-N) and the XXL South (XXL-S). Furthermore, it is the largest *XMM-Newton* project approved to date (>6 Ms) with median exposure at 10.4 ks and a depth of ∼6×10^{-15} erg s^{-1} cm^{-2} for point sources at the 90% completeness limit in the [0.5−2] keV band (XXL paper I). In this study, we use the XXL-N sample that consists of 14 168 sources, including extended objects. To identify the X-ray detections at other wavelengths the X-ray counterparts have been crossmatched with optical, NIR, and MIR surveys (for more details see Chiappetti et al. 2018, hereafter XXL paper XXVII).

2.2. Infrared AGN candidates

WISE (Wright et al. 2010) completed an all-sky coverage in four MIR bands: 3.4, 4.6, 12, and 22 μm ($W1$, $W2$, $W3$ and $W4$ bands, respectively). Various colour criteria used these IR bands to efficiently identify AGN candidates. For instance, Mateos et al. (2012) suggested a selection method using three WISE colours. Stern et al. (2012) used the $W1$ and $W2$ bands and applied the criterion $W1 - W2 \geq 0.8$ to select AGNs with $W2 < 15.05$ in the COSMOS field. Assef et al. (2013) extended the latter criterion and provided a selection of AGNs for fainter WISE sources using the WISE All-Sky data release catalogue. Assef et al. (2018) modified these criteria to incorporate data obtained during the post-cryogenic main mission extension (AllWISE catalogue).

In this study, we use approximately 500 000 WISE detections included in the latest WISE catalogue (AllWISE) that lie within the XMM-XXL area to select IR AGN candidates, applying the criteria of Assef et al. (2018). Specifically, we use

$$W1 - W2 \geq \alpha_R, \quad W2 \leq \gamma_R, \tag{1}$$

$$W1 - W2 > \alpha_R \exp[\beta_R (W2 - \gamma_R)^2], \quad W2 > \gamma_R, \tag{2}$$

where $(\alpha_R, \beta_R, \gamma_R) = (0.650, 0.153, 13.86)$, to select AGNs with 90% reliability.

2.3. Red AGNs

To select optically red sources from the IR AGN candidates, we apply the Yan et al. (2013) criterion ($r - W2 > 6$). This analysis reveals 561 red AGNs. We cross-match this subsample with the XXL catalogue to identify the X-ray counterparts of these sources. For the cross-match, we use a radius of 3 arcsec. Within this radius and given the X-ray source sky density, we find that a fraction of ∼0.2% of spurious matches is expected (Mountrichas et al. 2017). To study the X-ray absorption of the optically red AGN population, we apply an X-ray spectral fitting analysis. As one of our main goals is to quantify the obscuration in the red AGNs, we chose to analyse only the X-ray spectra of the sources with reliable photon statistics. For this reason, we keep only the sources with 50 or more net counts per detector (see Corral et al. 2015). There are 47 red AGNs that meet the aforementioned X-ray criteria. Table 1 presents the number of sources in the various subsamples. Table 2 presents the identity (ID), the redshift, and the r and $W2$ magnitudes in the

Table 2. General properties of the red AGN sample.

Object	3XLSS ID	Redshift	r (Vega)	W_2 (Vega)
1	J021835.7−053758	0.387	19.84	13.56
2	J022848.4−044426	1.046	21.14	15.03
3	J022928.4−051124	0.307	17.76	11.65
4	J022809.0−041235	0.879	19.46	13.01
5	J020654.9−064552	1.412	21.12	14.82
6	J020410.4−063924	0.414	21.83	14.65
7	J023315.5−054747	0.598	20.91	13.70
8	J021337.9−042814	0.419	18.54	12.17
9	J020436.4−042833	0.827	19.77	13.46
10	J020543.0−051656	0.653	20.78	13.93
11	J020517.3−051024	0.792	21.05	14.92
12	J022244.3−030525	0.637	21.74	14.39
13	J022323.4−031157	0.691	20.42	13.90
14	J022209.6−025023	0.400	21.36	14.51
15	J022750.7−052232	0.804	22.26	13.98
16	J022758.4−053306	0.956	21.49	13.74
17	J022453.2−054050	0.488	20.76	13.32
18	J022258.8−055757	0.732	21.60	13.70
19	J021844.6−054054	0.671	21.19	13.88
20	J021523.2−044337	0.860	19.96	13.21
21	J022321.9−045739	0.779	21.34	13.83
22	J022443.6−050905	0.943	21.55	14.93
23	J023418.0−041833	0.582	22.57	15.07
24	J020543.7−063807	0.772	22.72	14.79
25	J022932.6−055438	1.263	19.70	13.53
26	J021239.2−054816	0.711	22.32	15.10
27	J021511.4−060805	0.772	22.34	14.19
28	J021808.8−055630	0.572	20.05	14.06
29	J022538.9−040821	0.733	21.28	14.68
30	J020845.1−051354	*1.46*	23.39	15.16
31	J020953.9−055102	0.642	20.91	14.11
32	J020806.6−055739	0.539	21.34	13.83
33	J021509.0−054305	*0.70*	22.48	14.53
34	J021512.9−060558	*1.14*	23.36	15.14
35	J020529.5−051100	*1.20*	23.40	14.94
36	J022404.0−035730	*0.17*	22.79	14.88
37	J023501.0−055234	*0.85*	22.49	15.06
38	J020210.6−041129	*2.71*	21.09	14.08
39	J022650.3−025752	*1.21*	22.79	14.63
40	J021303.7−040704	*1.35*	22.20	15.32
41	J023357.7−054819	*1.60*	24.20	14.69
42	J020335.0−064450	*0.67*	23.28	15.05
43	J020823.4−040652	*2.23*	24.68	14.92
44	J020135.4−050847	*0.73*	23.14	15.16
45	J021837.2−060654	0.943	21.47	15.11
46	J022149.9−045920	*1.461*	23.05	14.79
47	J020311.3−063534	*1.05*	22.96	15.19

Notes. r is the SDSS photometric band (SDSS DR15; Aguado et al. 2019). r and W_2 magnitudes are on the Vega system. We use three decimal points for spectroscopic redshifts and photometric redshifts are in italics with two decimal points.

Vega system for the 47 optically red AGNs. In addition to optical and MIR photometry, 45 out of the 47 optically red AGNs have also been detected in the NIR (VISTA; Emerson et al. 2006; Dalton et al. 2006). The XXL field has been observed by the SPIRE instrument onboard *Herschel* mission at far-infrared (FIR) wavelengths (Oliver 2012). To identify the FIR counterparts, we used the ARCHES cross-correlation tool XMATCH

(Pineau et al. 2017). The details of the cross-match procedure are given in Sect. 2.2 of Masoura et al. (2018). We find nine sources with *Herschel* photometry. Finally, optical spectra are available for 33 out of the 47 red AGNs. The vast majority of them (30 out of 33) come from the SDSS (DR15) survey. The remaining optical spectra are from the Galaxy And Mass Assembly (GAMA; Driver et al. 2011; Baldry et al. 2010) and the VIPERS (Guzzo et al. 2014; Scodeggio et al. 2018) surveys. In our analysis, we use spectroscopic redshifts for 33 sources. For the remaining AGNs we use their photometric redshifts, estimated in Fotopoulou et al. (2016, hereafter XXL paper VI). The photometric redshift accuracy is 0.095 (for the full XMM-XXL catalogue). In our analysis, we incorporate the full probability density function (PDF) of the photometric redshifts when we calculate the uncertainties of the various parameters.

3. Analysis

We classify the 47 optically red AGNs of our sample as obscured or unobscured using different criteria. Specifically, we examine their X-ray spectra, SEDs, and optical spectra.

3.1. X-ray spectra

We examine the X-ray absorption of the 47 red AGNs in our sample. To achieve that, we apply X-ray spectral-fitting using the XSPEC v12.10 software (Arnaud 1996). We use the Cash statistical analysis (C-stat; Cash 1979) on the spectra binned to 1 count/bin, which has been shown to recover the actual spectral parameters in the most accurate way even for very low-count spectra (e.g. Krumpe et al. 2008). The model applied to the spectral data is a simple power law, $A(E) = KE^{-\Gamma}$, absorbed by both the Galactic photoelectric absorption and the intrinsic absorption. Γ is the photon index of the power law and K is the flux at 1 keV in units of photons $\mathrm{keV^{-1}\,cm^{-2}\,s^{-1}}$. The Galactic absorption is taken from the Leiden/Argentine/Bonn (LAB) Survey of Galactic HI Kalberla et al. (2005). The X-ray spectra for the 47 AGNs are presented in Figs. A.1–A.47. The best-fit values are presented in Table 3. In Fig. 1 we present N_H versus X-ray luminosity.

Figure 2 presents the N_H distribution of the sources, taking into account the N_H upper limits (Isobe et al. 1986). For that purpose, we use the Astronomical SURVival Statistics (ASURV; Lavalley et al. 1992) software package, which adopts the maximum-likelihood Kaplan-Meier estimator to take into account censored data (Feigelson & Nelson 1985). The derived mean value is log $N_H/\mathrm{cm^{-2}} = 21.80 \pm 0.13$. The distribution shows that the red sources are almost equally divided between obscured ($N_H > 10^{22}\,\mathrm{cm^{-2}}$) and unobscured AGNs. The limit of $N_H = 10^{22}\,\mathrm{cm^{-2}}$ is often used in X-rays because lower column densities can be produced by dust lanes in the galaxy instead of the torus (Malkan et al. 1998). However, we note that Merloni et al. (2013) propose an alternative dividing line of $3 \times 10^{21}\,\mathrm{cm^{-2}}$ in the sense that this provides a much better agreement when compared with the optical classification between Type-1 and Type-2 AGNs. From Figs. 1 and 2 it appears that the red $r−W2$ colour alone cannot guarantee that the source will be classified as obscured in X-rays.

3.2. SED fitting

We calculate the contribution of the AGNs to the power output of the host galaxy using the Code Investigating GALaxy

Table 3. X-ray properties of the red AGN sample.

Object	3XLSS ID	$N_{\rm H} \times 10^{22}\,{\rm cm}^{-2}$	$N_{\rm H} \times 10^{22}\,{\rm cm}^{-2}$ $\Gamma = 1.8$	Γ	$\log L_{\rm X}$ (2−10 keV) (erg s^{-1})	C-stat/d.o.f.
1	J021835.7−053758	$0.15^{+0.06}_{-0.06}$	–	$1.85^{+0.15}_{-0.15}$	8.7×10^{43}	802/1027
2	*J022848.4−044426*	<1.46	–	$1.77^{+1.40}_{-0.60}$	1.1×10^{44}	33/38
3	**J022928.4−051124**	$1.60^{+0.10}_{-0.08}$	–	$2.24^{+1.20}_{-0.30}$	2.9×10^{43}	512/578
4	J022809.0−041235	$0.14^{+0.12}_{-0.11}$	–	$1.87^{+0.21}_{-0.20}$	1.8×10^{45}	488/577
5	J020654.9−064552	<0.23	–	$1.75^{+0.26}_{-0.25}$	3.8×10^{43}	103/155
6	*J020410.4−063924*	$0.81^{+0.89}_{-0.68}$	–	$1.86^{+0.70}_{-0.58}$	7.8×10^{43}	106/138
7	J023315.5−054747	<0.62	–	$1.94^{+0.70}_{-0.40}$	3.2×10^{43}	89/107
8	**J021337.9−042814**	$12.1^{+7.20}_{-5.37}$	–	$1.60^{+0.60}_{-0.30}$	4.8×10^{43}	63/70
9	J020436.4−042833	<0.45	–	$1.86^{+0.25}_{-0.24}$	3.7×10^{44}	510/550
10	**J020543.0−051656**	<48.0	–	$1.80^{+8.10}_{-1.50}$	4.4×10^{43}	17/18
11	*J020517.3−051024*	$0.78^{+1.10}_{-0.70}$	–	$1.24^{+3.10}_{-0.90}$	2.5×10^{44}	22/46
12	**J022244.3−030525**	$23.8^{+18.30}_{-12.70}$	–	$1.51^{+1.20}_{-1.0}$	1.4×10^{44}	112/117
13	**J022323.4−031157**	$17.4^{+23.60}_{-13.00}$	–	$2.70^{+0.40}_{-0.20}$	7.4×10^{43}	27/39
14	*J022209.6−025023*	$0.80^{+0.40}_{-0.30}$	–	$1.90^{+0.40}_{-0.30}$	3.5×10^{43}	211/270
15	**J022750.7−052232**	$5.00^{+3.10}_{-2.00}$	–	$2.40^{+0.80}_{-0.70}$	1.2×10^{44}	154/179
16	J022758.4−053306	<0.10	–	$1.40^{+0.90}_{-0.50}$	1.6×10^{44}	33/44
17	**J022453.2−054050**	$5.80^{+4.20}_{-3.00}$	–	$1.40^{+0.70}_{-0.20}$	3.4×10^{43}	56/66
18	J022258.8−055757	<0.20	–	$1.60^{+2.60}_{-0.90}$	5.0×10^{43}	65/69
19	J021844.6−054054	<0.74	–	$1.80^{+0.70}_{-0.40}$	1.1×10^{44}	146/157
20	J021523.2−044337	<0.28	–	$2.10^{+0.80}_{-0.20}$	3.6×10^{43}	130/141
21	**J022321.9−045739**	$15.10^{+3.1}_{-1.40}$	–	$1.67^{+2.80}_{-1.80}$	1.5×10^{44}	93/92
22	*J022443.6−050905*	<1.10	–	$1.33^{+0.48}_{-0.35}$	8.1×10^{43}	142/172
23	J023418.0−041833	<0.40	–	$1.84^{+0.36}_{-0.45}$	2.3×10^{43}	15/16
24	**J020543.7−063807**	< 3.90	$8.1^{+2.2}_{-5.0}$	$1.18^{+0.54}_{-0.36}$	6.5×10^{44}	135/145
25	J022932.6−055438	<0.43	–	$1.50^{+0.50}_{-0.40}$	2.3×10^{44}	62/82
26	**J021239.2−054816**	$11.40^{+0.30}_{-0.20}$	–	$1.80^{+0.60}_{-0.20}$	6.0×10^{43}	10/11
27	**J021511.4−060805**	<22	$16.0^{+3.8}_{-9.2}$	$1.00^{+1.80}_{-1.50}$	2.4×10^{44}	48/50
28	J021808.8−055630	$0.16^{+0.07}_{-0.06}$	–	$1.98^{+0.22}_{-0.24}$	9.2×10^{43}	92/104
29	**J022538.9−040821**	$4.95^{+4.80}_{-4.30}$	–	$1.60^{+0.80}_{-0.30}$	2.3×10^{43}	31/34
30	*J020845.1−051354*	<1.00	–	$1.90^{+0.70}_{-0.40}$	2.5×10^{44}	73/89
31	**J020953.9−055102**	<28	–	$1.60^{+0.6}_{-0.8}$	8.7×10^{43}	37/30
32	**J020806.6−055739**	$1.80^{+0.30}_{-0.18}$	–	$2.30^{+1.20}_{-0.40}$	2.0×10^{43}	80/56
33	**J021509.0−054305**	<33.00	–	$1.33^{+3.10}_{-1.90}$	3.3×10^{43}	30/28
34	*J021512.9−060558*	<1.70	–	$1.71^{+0.70}_{-0.50}$	1.7×10^{44}	103/123
35	*J020529.5−051100*	<1.47	–	$1.35^{+0.80}_{-0.40}$	1.6×10^{44}	86/90
36	**J022404.0−035730**	$5.30^{+7.15}_{-3.09}$	–	$1.82^{+0.40}_{-0.70}$	9.3×10^{43}	52/59
37	*J023501.0−055234*	<5.40	–	$1.42^{+0.30}_{-0.60}$	3.5×10^{43}	33/23
38	*J020210.6−041129*	<4.20	–	$1.22^{+0.90}_{-0.40}$	1.8×10^{45}	8/12
39	**J022650.3−025752**	$9.00^{+1.37}_{-2.94}$	–	$1.83^{+0.8}_{-0.4}$	3.5×10^{44}	56/70
40	**J021303.7−040704**	<14.0	$19.2^{+3.9}_{-3.0}$	$0.70^{+1.10}_{-0.80}$	1.8×10^{44}	32/46
41	*J023357.7−054819*	<2.30	–	$1.60^{+0.40}_{-0.40}$	1.1×10^{45}	192/259
42	*J020335.0−064450*	<2.50	–	$1.50^{+1.38}_{-0.42}$	5.4×10^{43}	44/57
43	**J020823.4−040652**	<0.50	$1.9^{+0.6}_{-1.6}$	$1.20^{+1.00}_{-0.70}$	3.2×10^{44}	55/58
44	J020135.4−050847	<0.81	–	$1.35^{+0.80}_{-0.30}$	5.6×10^{43}	86/90
45	*J021837.2−060654*	$0.93^{+0.05}_{-0.28}$	–	$2.00^{+0.40}_{-0.30}$	3.8×10^{43}	158/172
46	**J022149.9−045920**	<1.70	$2.6^{+0.5}_{-1.2}$	$1.10^{+1.20}_{-0.80}$	3.1×10^{42}	40/49
47	**J020311.3−063534**	$3.20^{+14.42}_{-2.85}$	–	$1.60^{+1.50}_{-0.90}$	9.3×10^{43}	20/30

Notes. When $\Gamma \leq 1.2$, we quote the $N_{\rm H}$ estimations with Γ fixed to $\Gamma = 1.8$ and present the $N_{\rm H}$ estimations in Col. 4. Sources classified as X-ray obscured based on our strict criteria (see text for more details) are presented in bold. Sources that satisfy the loosened X-ray criteria (see text) are shown in italics. The energy band of $L_{\rm X}$ is [2−10 keV].

Emission (CIGALE; Burgarella et al. 2005; Noll et al. 2009). We provide the CIGALE code version 2018.0 with multiwavelength flux densities, using optical, NIR, and MIR photometry. Table 4 presents the models and the parameters used by CIGALE for the SED fitting of our X-ray sample. The Fritz et al. (2006) library of templates was used to model the AGN emission. The AGN fraction is measured as the AGN emission relative to IR luminosity (1−1000 μm). Here, τ is the e-folding time of the main stellar population model in millions of years. Age is defined as the age of the main stellar population, also in millions of years. The extinction of a source is derived from the viewing angle, Ψ, of the torus: Ψ ≤ 30° for Type 2 (edge-on),
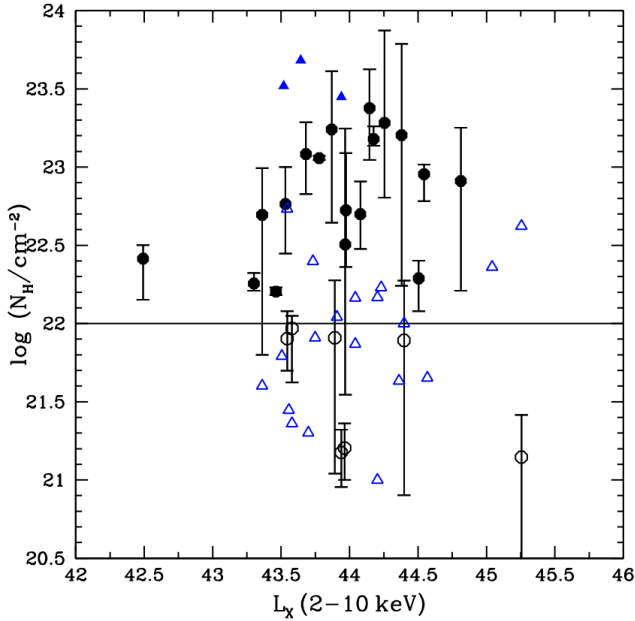
Fig. 1. N_H as a function of X-ray luminosity for the 47 optical red AGNs. Those sources for which the X-ray spectral fitting could not constrain their N_H are presented with a triangle (upper limit estimations). The 21 AGNs that satisfy our X-ray absorption criteria are presented with filled symbols (see text for more details).

Fig. 2. N_H distribution taking into account N_H upper limits; see text for more details.

$40° \leq \Psi \leq 60°$ for intermediate, and $\Psi \geq 70°$ for Type 1 AGNs (face-on; Ciesla et al. 2015), respectively. No intermediate values are used. The results from these fits appear in Table 5 and the SEDs are shown in Figs. A.1–A.47 (for more details on the SED fitting, see also Masoura et al. 2018).

As mentioned in the previous section, *Herschel* photometry is available for nine of the sources in our sample. We fit the SEDs of these sources with and without FIR data to check whether the lack of FIR photometric bands affects the SED fitting measurements. Specifically, we are interested in the inclination angle Ψ, since this parameter is used as a proxy to determine the obscuration of an AGN. We find that the inclusion of FIR photometry in the SED fitting does not change the AGN emission or the estimated inclination angle of the sources. Thus, we conclude that a lack of FIR photometry for the remaining sources does not affect our analysis.

3.3. Optical spectra

The optical spectra for 33 out of 47 sources are presented in Figs. A.1–A.47. Optically unobscured sources (Type 1) are considered to be those with broad emission lines (BL), whereas obscured sources (Type 2) exhibit only narrow emission lines (NL) or a red continuum. The AGNs are characterised as obscured, unobscured, or intermediate (IMD) type, based on visual inspection of their optical spectra. Table 6 contains the classification according to the optical spectrum for each object.

To verify the redshift of our sources and assess their obscuration in the optical band we used the optical spectra provided by the SDSS. We recomputed the spectroscopic redshift and for a small number of cases we provide in Table 2 a different measurement from the one in SDSS.

4. Discussion

Our IR selection criteria identify 4798 AGN candidates (Table 1). Of these, 2652 have been observed by SDSS.
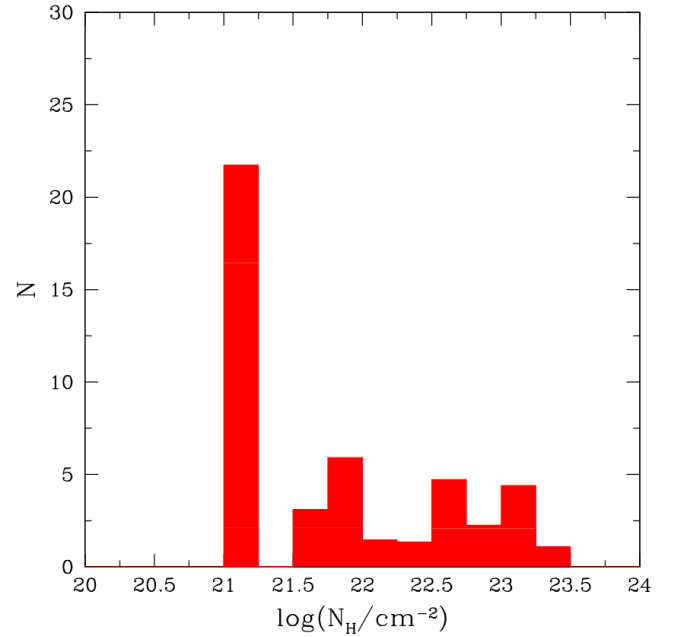
Approximately 20% of these sources are optically red using the criteria of Yan et al. (2013); see Table 1. Figures 3 and 4 show the i-band and the $r-W2$ distributions of the various samples. As expected, red sources occupy the faint part of the i-band distribution while the AGN sample with available X-ray spectra lacks sources with the highest $r-W2$ values.

In our analysis, we explore the X-ray spectral properties of the 47 optically red AGNs and examine whether these sources are also X-ray absorbed. Furthermore, we search for indications of extinction either on their SEDs or in their optical spectra. The results of the X-ray spectral fitting are presented in Table 3. For those cases where the photon index (Γ) is unphysically low ($\Gamma < 1.2$) we quote the N_H estimations with Γ fixed to $\Gamma = 1.8$ (Nandra & Pounds 1994). The latter N_H estimation is used to characterise the X-ray absorption of the source. Our analysis reveals 18 sources with best-fit intrinsic column densities $N_H > 10^{22}$ cm^{-2}. We also consider as possibly absorbed a source whose upper limit lies above the arbitrary chosen limit of $N_H = 10^{23}$ cm^{-2} (i.e. J020543.0−051656, J020953.9−055102, J021509.0−054305). The latter increases the number of candidate X-ray-absorbed sources to 21. We characterise these systems as X-ray-absorbed sources and mark them in bold in Table 7. However, there are AGNs that present mild absorption and could be classified as X-ray absorbed if we eased our X-ray criteria. Thus, lowering our X-ray absorption criteria, that is, $N_H > 10^{21.5}$ cm^{-2} (Merloni et al. 2013) or upper limit that lies above the N_H value $N_H = 10^{22}$ cm^{-2}, we find 13 additional sources that present signs of X-ray absorption. These additional sources are shown in italics in Table 7. Therefore, up to 34 AGNs (72%) in the sample present some signs of X-ray absorption.

The vast majority of our optically red AGNs have SEDs that show clear signs of obscuration in their AGN emission (green lines is Figs. A.1–A.47). However, the AGN emission of the source J022809.0−041235 (no. 4 in Table 5) extends to the optical part of the spectrum without presenting signs of even mild obscuration. This source has also large Ψ ($\Psi = 80°$) that also indicates a Type 1 AGN (X-ray and optical spectra also confirm this is an unobscured AGN). There are two more sources

Table 4. Models and values for their free parameters used by CIGALE for the SED fitting of our X-ray samples.

Parameter	Model/values
Stellar population synthesis model	
Initial mass function	Salpeter
Metallicity	0.02 (Solar)
Single stellar population library	Bruzual & Charlotte (2003)
Double exponentially decreasing (2τ dec) model	
τ	100, 1000, 5000, 10000
Age	500, 2000, 5000, 10000, 12000
Burst age	100, 200, 400
Dust extinction	
Dust attenuation law	Calzetti et al. (2000)
Reddening $E(B-V)$	0.01, 0.1, 0.3, 0.5, 0.8, 1.2
$E(B-V)$ reduction factor between old and young stellar population	0.44
Fritz et al. (2006) model for AGN emission	
Ratio between outer and inner dust torus radii	10, 60, 150
$9.7\,\mu$m equatorial optical depth	0.1, 0.3, 1.0, 2.0, 6.0, 10.0
β	-0.5
γ	0.0, 2.0, 6.0
Θ	100°
Ψ	0°, 10°, 20°, 30°, 40°, 50°, 60°, 70°, 80°, 90°
AGN fraction	0.1, 0.2, 0.3, 0.4, 0.5, 0.6, 0.7, 0.8, 0.9

Notes. τ is the e-folding time of the main stellar population model in Myr, age is defined as the age of the main stellar population in the galaxy in Myr, and burst age is the age of the late burst in Myr. Here, β and γ are the parameters used to define the law for the spatial behaviour of density of the torus density. The functional form of the latter is $\rho(r,\theta) \propto r^{\beta} e^{-\gamma|\cos\theta|}$, where r and θ are the radial distance and the polar distance, respectively. Θ is the opening angle and Ψ the viewing angle of the torus. Type 2 AGNs have $\Psi \leq 30°$ (edge-on) and Type 1 AGN have $\Psi \geq 70°$ (face-on). $40° \leq \Psi \leq 60°$ corresponds to intermediate-type AGNs. The AGN fraction is measured as the AGN emission relative to IR luminosity $(1-1000\,\mu$m).

with a large Ψ value (i.e. observed face-on), namely sources J020517.3−051024 and J021808.8−055630 (nos. 11 and 28 in Table 5). Their SEDs reveal that even though the AGN emission extends to the optical part of the SED, the emission of the galaxy is a dominant component of the SED at the optical wavelengths. We refer to the latter two systems as galaxy dominated. We attribute this term to sources that satisfy the following criteria: (i) the IR ($W2$) emission of the system is due to the AGN emission, and (ii) there is a strong galaxy emission in the optical part of the SED even though the AGN emission is only mildly obscured (or not obscured at all). Specifically, the ratio of the galaxy emission to the AGN emission in the r band is ≥ 1. Although source no. 28 is not X-ray absorbed, source no. 11 presents signs of mild X-ray absorption ($N_{\rm H} = 0.78^{+1.10}_{-0.70} \times 10^{22}\,$cm^{-2}). The optical spectra of these two systems have broad emission lines, corroborating the assertion that these are unobscured sources. We conclude that the SEDs for 44 out of the 47 sources in our sample present clear signs of obscuration based on their AGN emission and their Ψ values.

In addition to these two AGNs (i.e. sources 11 and 28 in Table 5), there are eight more sources that satisfy our aforementioned criteria and are therefore considered galaxy-dominated systems (nos. 5, 7, 10, 26, 35, 39, 44, and 47). In these systems, the galaxy and/or AGN emission in the r band ranges from ≈ 1 (e.g. no. 28) to ≥ 10 (e.g. nos. 10, 39, and 47). Five of these sources are among the AGNs that are also X-ray absorbed (nos. 10, 26, 35, 39, and 47 in Table 7). Their AGN fraction, frac$_{\rm AGN}$ = 40−80% (Table 5). These suggest that these systems are galaxy dominated because the AGN is obscured and not because the active SMBH is intrinsically weak. However, for the remaining three galaxy-dominated systems (nos. 5, 7, and 44) that are not X-ray absorbed, it could be that they are

characterised as optically red ($r-W2 > 6$) due to an intrinsically weak AGN (AGN fraction, frac$_{\rm AGN}$ = 20−30%, Table 5) rather than an obscured AGN. Galaxy-dominated systems are known to confuse optical and MIR criteria (Koutoulidis et al. 2018).

Excluding the ten galaxy-dominated systems from our sample of red IR AGNs reduces the total number of red sources to 37. Of these, 17 (46% of the total sample) and 28 (76% of the total sample) are X-ray absorbed using the strict and loose criteria, respectively. Therefore, there are nine ($\sim$20%) IR red AGNs in our sample that present no signs of X-ray absorption. The optical spectra for two of these sources present narrow emission lines (nos. 16 and 20 in Table 7), four present broad emission lines (nos. 1, 3, 9, and 25 in Table 7) and two are of intermediate type (nos. 17 and 18 in Table 7) based on our visual inspection. The optical spectrum of source no. 23 is too noisy to extract any information. Previous studies have found that selection of obscured AGNs based on optical and/or MIR colours are 80% reliable (Hickox et al. 2007). This could explain why at least some of these nine AGNs, although optically red, present broad emission lines in their spectra and no substantial X-ray absorption.

Recently, Jaffarian & Gaskell (2020) studied the optical $E(B-V)$ reddening versus the X-ray absorbing column density for a large sample of Seyfert galaxies with both $E(B-V)$ and X-ray absorption column density measurements. These latter authors find a significant correlation between $E(B-V)$ and $N_{\rm H}$, albeit with a large scatter of $\pm$dex, which they claim could be attributed to X-ray column density variability. Regardless of the origin of the physical interpretation, the presence of such a large scatter can readily explain why some of our red sources show no sign of significant absorption in X-rays. The fact that the average absorbing column density derived for the red $r-W2 > 6$

Table 5. SED properties of the red AGN sample.

Object	3XLSS ID	Ψ (deg)	frac$_{AGN}$	χ^2_{red}
1	J021835.7−053758	20	$0.30^{+0.10}_{-0.10}$	0.43
2	J022848.4−044426	40	$0.30^{+0.10}_{-0.10}$	6.35
3	J022928.4−051124	20	$0.40^{+0.10}_{-0.10}$	4.42
4	J022809.0−041235	80	$0.30^{+0.15}_{-0.15}$	1.52
5	J020654.9−064552	20	$0.30^{+0.15}_{-0.15}$	4.23
6	J020410.4−063924	40	$0.50^{+0.15}_{-0.15}$	2.99
7	J023315.5−054747	20	$0.30^{+0.10}_{-0.10}$	0.48
8	J021337.9−042814	10	$0.60^{+0.05}_{-0.05}$	2.50
9	J020436.4−042833	20	$0.60^{+0.15}_{-0.15}$	3.17
10	J020543.0−051656	20	$0.50^{+0.05}_{-0.05}$	0.47
11	J020517.3−051024	70	$0.20^{+0.10}_{-0.10}$	5.09
12	J022244.3−030525	40	$0.40^{+0.15}_{-0.15}$	0.43
13	J022323.4−031157	20	$0.40^{+0.20}_{-0.20}$	3.00
14	J022209.6−025023	30	$0.30^{+0.15}_{-0.15}$	2.71
15	J022750.7−052232	10	$0.30^{+0.10}_{-0.10}$	3.28
16	J022758.4−053306	0	$0.60^{+0.05}_{-0.05}$	3.13
17	J022453.2−054050	10	$0.40^{+0.15}_{-0.15}$	0.70
18	J022258.8−055757	20	$0.50^{+0.05}_{-0.05}$	2.72
19	J021844.6−054054	30	$0.70^{+0.10}_{-0.10}$	1.82
20	J021523.2−044337	30	$0.50^{+0.15}_{-0.15}$	3.04
21	J022321.9−045739	30	$0.60^{+0.10}_{-0.10}$	2.65
22	J022443.6−050905	10	$0.30^{+0.10}_{-0.10}$	0.56
23	J023418.0−041833	10	$0.70^{+0.20}_{-0.20}$	2.42
24	J020543.7−063807	40	$0.60^{+0.10}_{-0.10}$	0.13
25	J022932.6−055438	10	$0.60^{+0.10}_{-0.10}$	1.25
26	J021239.2−054816	50	$0.80^{+0.20}_{-0.20}$	3.34
27	J021511.4−060805	10	$0.70^{+0.20}_{-0.20}$	1.02
28	J021808.8−055630	80	$0.30^{+0.10}_{-0.10}$	2.30
29	J022538.9−040821	10	$0.40^{+0.10}_{-0.10}$	1.30
30	J020845.1−051354	50	$0.30^{+0.10}_{-0.10}$	1.28
31	J020953.9−055102	30	$0.60^{+0.10}_{-0.10}$	2.68
32	J020806.6−055739	40	$0.60^{+0.10}_{-0.10}$	0.92
33	J021509.0−054305	30	$0.70^{+0.20}_{-0.20}$	4.89
34	J021512.9−060558	0	$0.80^{+0.10}_{-0.10}$	0.18
35	J020529.5−051100	10	$0.50^{+0.20}_{-0.20}$	4.19
36	J022404.0−035730	20	$0.30^{+0.20}_{-0.20}$	0.60
37	J023501.0−055234	10	$0.30^{+0.20}_{-0.20}$	0.37
38	J020210.6−041129	10	$0.30^{+0.05}_{-0.05}$	1.46
39	J022650.3−025752	40	$0.50^{+0.20}_{-0.20}$	1.67
40	J021303.7−040704	30	$0.80^{+0.10}_{-0.10}$	0.19
41	J023357.7−054819	10	$0.70^{+0.10}_{-0.20}$	0.62
42	J020335.0−064450	10	$0.70^{+0.20}_{-0.20}$	0.03
43	J020823.4−040652	10	$0.80^{+0.10}_{-0.10}$	0.53
44	J020135.4−050847	20	$0.20^{+0.20}_{-0.10}$	0.62
45	J021837.2−060654	20	$0.40^{+0.20}_{-0.20}$	1.00
46	J022149.9−045920	30	$0.80^{+0.10}_{-0.10}$	0.36
47	J020311.3−063534	10	$0.40^{+0.15}_{-0.15}$	0.16

Notes. We consider sources with $\Psi \leq 30°$ as Type 2 (edge-on), $40° \leq \Psi \leq 60°$ as intermediate and $\Psi \geq 70°$ as Type 1 AGNs, based on their best-fit values.

Table 6. Optical properties of the red AGN sample.

Object	3XLSS ID	Optical
1	J021835.7−053758	BL
2	J022848.4−044426	BL, flat
3	J022928.4−051124	BL
4	J022809.0−041235	BL, flat
5	J020654.9−064552	NL
6	J020410.4−063924	NL
7	J023315.5−054747	NL
8	J021337.9−042814	BL, blue
9	J020436.4−042833	BL
10	J020543.0−051656	BL
11	J020517.3−051024	BL
12	J022244.3−030525	NL, red
13	J022323.4−031157	IMD
14	J022209.6−025023	NL
15	J022750.7−052232	IMD
16	J022758.4−053306	NL
17	J022453.2−054050	IMD
18	J022258.8−055757	IMD
19	J021844.6−054054	IMD
20	J021523.2−044337	NL
21	J022321.9−045739	NL
22	J022443.6−050905	IMD
23	J023418.0−041833	Noisy
24	J020543.7−063807	Noisy
25	J022932.6−055438	BL
26	J021239.2−054816	Noisy
27	J021511.4−060805	NL
28	J021808.8−055630	BL
29	J022538.9−040821	BL
30	J020845.1−051354	–
31	J020953.9−055102	BL
32	J020806.6−055739	NL, red
33	J021509.0−054305	–
34	J021512.9−060558	–
35	J020529.5−051100	–
36	J022404.0−035730	–
37	J023501.0−055234	–
38	J020210.6−041129	–
39	J022650.3−025752	–
40	J021303.7−040704	–
41	J023357.7−054819	–
42	J020335.0−064450	–
43	J020823.4−040652	–
44	J020135.4−050847	–
45	J021837.2−060654	Noisy
46	J022149.9−045920	BL
47	J020311.3−063534	–

Notes. Optically unobscured sources (Type 1) are considered to be those with broad emission lines (BL). Whereas obscured sources (Type 2) exhibit only narrow emission lines (NL) or a red continuum. The AGNs are characterised as obscured, unobscured, or intermediate type (IMD) based on visual inspection of their optical spectra. We note that in the optical spectra of sources 13 and 22, while the MgII lines are broad, all other lines are narrow. This is attributed to the wider area from which the MgII originates with respect to the Balmer lines. These sources are characterized as IMD.

sources is only $N_H = 21.8 \pm 0.13$ suggests that the above obscuration criterion selects sources with lower absorption compared to those selected in X-rays using $N_H > 10^{22}$ cm^{-2} (e.g. Akylas et al. 2006; Ueda et al. 2014). In other words, the optically red source selection does not correspond to the same level of obscuring column densities as those seen for X-ray wave-

lengths. Hickox et al. (2017) proposed an additional criterion for the selection of obscured AGNs based on the combination of the u and WISE $W3$ band. Since there is not a unique definition of how obscured an AGN must be to be classified as absorbed, the various selection criteria target different ranges of obscura-
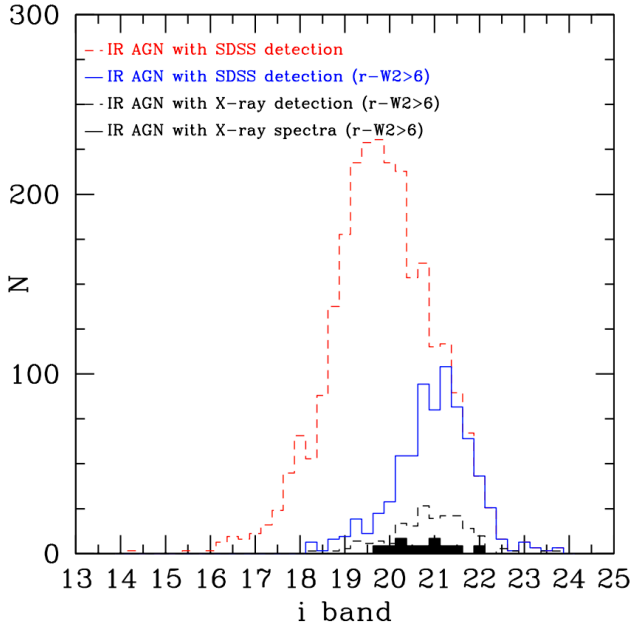
Fig. 3. *i*-band distribution of our sample. Red sources occupy the faint part of the *i*-band distribution.
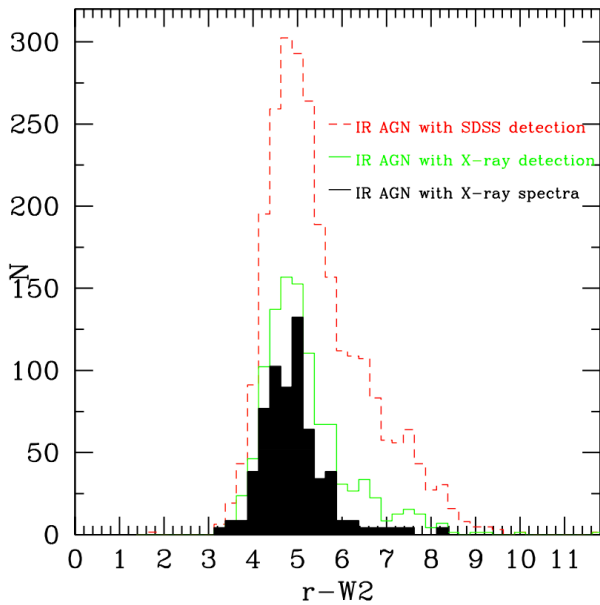
Fig. 4. $r-W2$ distribution of our sample. The AGN sample with available X-ray spectra lacks sources with the highest $r-W2$ values.

tion. Specifically, the application of the "usual" X-ray criterion $N_H > 10^{22}\,cm^{-2}$ selects the most obscured part of the obscured AGN distribution, while the $r-W2$ criterion extends to lower levels of obscuration. Finally, the Hickox et al. $u-W3$ criterion is sensitive to the lowest levels of obscuration. This is due to the use of the u band that is easily affected by even small amounts of reddening. The different selection criteria indeed result in different obscured AGN samples. This is most probably the reason why only 76% (at most) of the red AGN sample is absorbed in X-rays with column densities log $N_H/cm^{-2} > 21.5$.

5. Summary

Here, we applied the Assef et al. (2018) criteria based on the $W1$ and $W2$ WISE bands to select IR AGNs in the XXL-North

Table 7. Comparison of the X-ray, SED, and optical properties.

Object	ID 3XLSS	Classification		
		Xray	SED	optical
1	J021835.7−053758	1	2	1
2	*J022848.4−044426*	2	2	1
3	**J022928.4−051124**	2	2	1
4	J022809.0−041235	1	1	1
5	J020654.9−064552	1	2	2
6	*J020410.4−063924*	2	2	2
7	J023315.5−054747	1	2	2
8	**J021337.9−042814**	2	2	1
9	J020436.4−042833	1	2	1
10	**J020543.0−051656**	2	2	1
11	*J020517.3−051024*	2	1	1
12	**J022244.3−030525**	2	2	2
13	**J022323.4−031157**	2	2	**3**
14	*J022209.6−025023*	2	2	2
15	**J022750.7−052232**	2	2	**3**
16	J022758.4−053306	1	2	2
17	**J022453.2−054050**	2	2	**3**
18	J022258.8−055757	1	2	**3**
19	J021844.6−054054	1	2	**3**
20	J021523.2−044337	1	2	2
21	**J022321.9−045739**	2	2	2
22	*J022443.6−050905*	2	2	**3**
23	J023418.0−041833	1	2	0
24	**J020543.7−063807**	2	2	0
25	J022932.6−055438	1	2	1
26	**J021239.2−054816**	2	2	0
27	**J021511.4−060805**	2	2	1
28	J021808.8−055630	1	1	1
29	**J022538.9−040821**	2	2	1
30	*J020845.1−051354*	2	2	–
31	**J020953.9−055102**	2	2	1
32	**J020806.6−055739**	2	2	2
33	**J021509.0−054305**	2	2	–
34	*J021512.9−060558*	2	2	–
35	*J020529.5−051100*	2	2	–
36	**J022404.0−035730**	2	2	–
37	*J023501.0−055234*	2	2	–
38	*J020210.6−041129*	2	2	–
39	**J022650.3−025752**	2	2	–
40	**J021303.7−040704**	2	2	–
41	*J023357.7−054819*	2	2	–
42	*J020335.0−064450*	2	2	–
43	**J020823.4−040652**	2	2	–
44	J020135.4−050847	1	2	–
45	*J021837.2−060654*	2	2	0
46	**J022149.9−045920**	2	2	2
47	**J020311.3−063534**	2	2	–

Notes. Sources classified as X-ray obscured based on our strict criteria (see text for more details) are presented in bold. Sources that satisfy the loosened X-ray criteria (see text) are shown in italics. Numbers 1 (unobscured) and 2 (obscured) are used to denote the classification of the sources based on the various criteria. Numbers 0 and 3 refer to optical spectra that are too noisy to allow us to classify them and are IMD type, respectively. The first number refers to the X-ray classification, while the second and the third numbers correspond to the SED- and optical-based characterisation.

25 deg^2 survey area. The above criteria yield 4798 AGNs. Moreover, we applied the optical MIR colour criterion $r-W2$ (Yan et al. 2013) in order to select obscured AGNs. We identify 561 red AGNs, of which 135 are detected in X-rays while 47 have good photon statistics (at least 50 net counts per detector), and derive a reliable estimate of the absorbing column

density. We used XSPEC to fit the X-ray spectra of the 47 sources and quantify their X-ray absorption. Of these 47 sources, 76% may show signs of absorption higher than $\log N_{\text{H}}/\text{cm}^{-2} = 21.5$. Furthermore, we applied the CIGALE code in order to study the SEDs of our 47 red sources. The SED analysis revealed that 10/47 sources are galaxy-dominated systems as the red colours are attributed to the host galaxy rather than absorption. In the vast majority of the remaining 37 sources, the SEDs confirm the presence of significant obscuration. The exact nature of the red sources that show low levels of X-ray absorption (25%) in apparent contradiction with their SEDs is unclear. The large scatter in the $r-W2$ colour versus column density, possibly caused by variability of the column density, is likely to offer an explanation. Our work shows that the $r-W2$ selection provides a robust method for selecting obscured AGNs. However, it may also identify sources that present lower levels of obscuration when compared with the widely used X-ray spectroscopic criteria which usually define obscured sources as those with $\log N_{\text{H}}/\text{cm}^{-2} > 21.5$.

References

Aguado, D. S., Hernández, J. I. G., Prieto, C. A., & Rebolo, R. 2019, ApJ, 874, L21
Akylas, A., Georgantopoulos, I., Georgakakis, A., Kitsionas, S., & Hatziminaoglou, E. 2006, A&A, 459, 693
Antonucci, R. 1993, ARA&A, 31, 473
Arnaud, K. A. 1996, ASP Conf. Ser., 101, 17
Assef, R. J., Stern, D., Kochanek, C. S., et al. 2013, ApJ, 772, 26
Assef, R. J., Stern, D., Noirot, G., et al. 2018, ApJS, 234, 23
Baldry, I. K., Robotham, A. S. G., Hill, D. T., et al. 2010, MNRAS, 404, 86
Bruzual, G., & Charlotte, S. 2003, MNRAS, 344, 1000
Burgarella, D., Buat, V., & Iglesias-Páramo, J. 2005, MNRAS, 360, 1413
Calzetti, D., Armus, L., Bohlin, R. C., et al. 2000, ApJ, 533, 682
Cash, W. 1979, ApJ, 228, 939
Chiappetti, L., Fotopoulou, S., Lidman, C., et al. 2018, A&A, 620, A12
Ciesla, L., Charmandaris, V., Georgakakis, A., et al. 2015, A&A, 576, A10
Civano, F., Elvis, M., Brusa, M., et al. 2012, ApJS, 201, 30
Corral, A., Georgantopoulos, I., Watson, M. G., et al. 2015, A&A, 576, A61
Cross, N. J. G., Collins, R. S., Mann, R. G., et al. 2012, A&A, 548, A119
Dalton, G. B., Caldwell, M., Ward, A. K., et al. 2006, Proc. SPIE, 6269, 62690X
Donoso, E., Yan, L., Stern, D., & Assef, R. J. 2014, ApJ, 789, 44
Driver, S. P., Hill, D. T., Kelvin, L. S., et al. 2011, MNRAS, 413, 971
Edelson, R. A., & Malkan, M. A. 1986, ApJ, 308, 59
Emerson, J., McPherson, A., & Sutherland, W. 2006, The Messenger, 126, 41
Feigelson, E. D., & Nelson, P. I. 1985, ApJ, 293, 192
Fiore, F., Puccetti, S., Brusa, M., et al. 2009, ApJ, 693, 447
Fotopoulou, S., Pacaud, F., Paltani, S., et al. 2016, A&A, 592, A5
Fritz, J., Franceschini, A., & Hatziminaoglou, E. 2006, MNRAS, 166, 767
Guzzo, L., Scodeggio, M., Garilli, B., et al. 2014, A&A, 566, A108
Haardt, F., & Maraschi, L. 1991, ApJ, 380, L51
Hambly, N. C., Collins, R. S., Cross, N. J. G., et al. 2008, MNRAS, 384, 637
Hickox, R., & Alexander, D. 2018, ARA&A, 56, 625
Hickox, R. C., Jones, C., Forman, W. R., et al. 2007, ApJ, 671, 1365
Hickox, R. C., Myers, A. D., Greene, J. E., et al. 2017, ApJ, 849, 53
Hönig, S. F., & Kishimoto, M. 2010, A&A, 523, A27
Hönig, S. F., & Kishimoto, M. 2017, ApJ, 838, L20
Hönig, S. F., Kishimoto, M., Gandhi, P., et al. 2010, A&A, 515, A23
Irwin, M. J., Lewis, J., Hodgkin, S., et al. 2004, Optimizing Scientific Return for Astronomy through Information Technologies (SPIE), 5493
Isobe, T., Feigelson, E. D., & Nelson, P. I. 1986, ApJ, 306, 490
Jaffarian, G. W., & Gaskell, C. M. 2020, MNRAS, 493, 930
Kalberla, P. M. W., Burton, W. B., Hartmann, D., et al. 2005, A&A, 440, 775
Kormendy, J., Bender, R., Ajhar, E. A., et al. 1996a, ApJ, 473, L91
Kormendy, J., Bender, R., Richstone, D., et al. 1996b, ApJ, 459, L57
Koutoulidis, L., Georgantopoulos, I., Mountrichas, G., et al. 2018, MNRAS, 481, 3063
Krumpe, M., Lamer, G., Corral, A., et al. 2008, A&A, 483, 415
LaMassa, S. M., Civano, F., Brusa, M., et al. 2016, ApJ, 818, 88
Lavalley, M., Isobe, T., & Feigelson, E. 1992, ASP Conf. Ser., 25, 245
Malkan, M. A., Gorjian, V., & Tam, R. 1998, ApJS, 117, 25
Masoura, V. A., Mountrichas, G., Georgantopoulos, I., et al. 2018, A&A, 618, A31
Mateos, S., Alonso-Herrero, A., Carrera, F. J., et al. 2012, MNRAS, 426, 3271
Merloni, A., Bongiorno, A., Brusa, M., et al. 2013, MNRAS, 437, 3550
Mountrichas, G., Georgantopoulos, I., Secrest, N. J., et al. 2017, MNRAS, 468, 3042
Nandra, K., & Pounds, K. A. 1994, MNRAS, 268, 405
Nenkova, M., Sirocky, M. M., Nikutta, R., Ivezić, Ž., & Elitzur, M. 2008a, ApJ, 685, 160
Nenkova, M., Sirocky, M. M., Ivezić, Ž., & Elitzur, M. 2008b, ApJ, 685, 147
Netzer, H. 2015, ARA&A, 53, 365
Noll, S., Burgarella, D., Giovannoli, E., et al. 2009, A&A, 507, 1793
Oliver, S. J., et al. 2012, MNRAS, 424, 1614
Pierre, M., Pacaud, F., Adami, C., et al. 2016, A&A, 592, A1
Pineau, F.-X., Derriere, S., Motch, C., et al. 2017, A&A, 597, A89
Scodeggio, M., Guzzo, L., Garilli, B., et al. 2018, A&A, 609, A84
Siebenmorgen, R., Heymann, F., & Efstathiou, A. 2015, A&A, 583, A120
Stalevski, M., Ricci, C., Ueda, Y., et al. 2016, MNRAS, 458, 2288
Stern, D., Assef, R. J., Benford, D. J., et al. 2012, ApJ, 753, 30
Ueda, Y., Akiyama, M., Hasinger, G., Miyaji, T., & Watson, M. G. 2014, ApJ, 786, 104
Ulrich, M.-H., Maraschi, L., & Urry, C. M. 1997, ARA&A, 35, 445
Wilkins, D. R., & Gallo, L. C. 2015, MNRAS, 448, 703
Wright, E. L., Eisenhardt, P. R. M., Mainzer, A. K., et al. 2010, AJ, 140, 1868
Yan, L., Donoso, E., Tsai, C.-W., et al. 2013, AJ, 145, 55

Appendix A: X-ray, optical spectra, and SEDs

In this section, we present the X-ray, SEDs, and the optical spectra (when available) for each one of the 47 optically red sources in our sample. Numbers 1 and 2 are used to denote the classification of the sources based on the various criteria. Specifically, 1 refers to unobscured and 2 to obscured sources. Number 0 is used in those cases where the optical spectrum is too noisy to extract any useful information. Number 3 is used to denote IMD type of classification. The numbers in parentheses refer to the classification based on the X-ray spectrum, the SED, and the optical spectrum, respectively. We use three decimal points for spectroscopic redshifts and two decimal points for photometric redshifts.

Fig. A.1. J021835.7−053758 (1,2,1), $z = 0.387$.
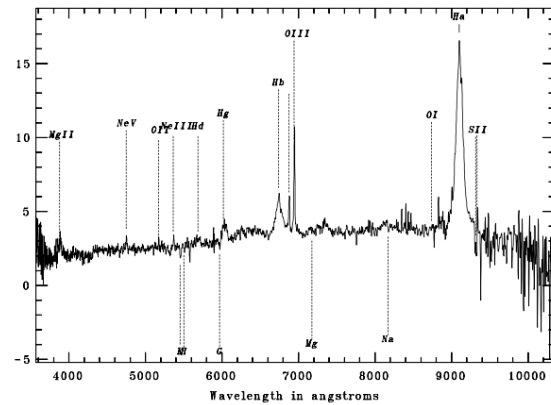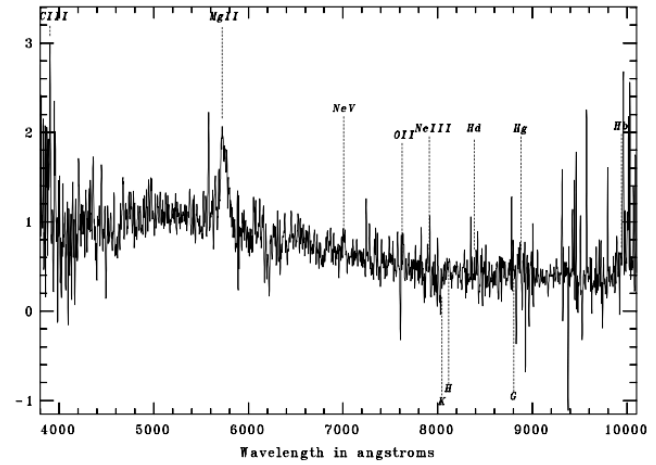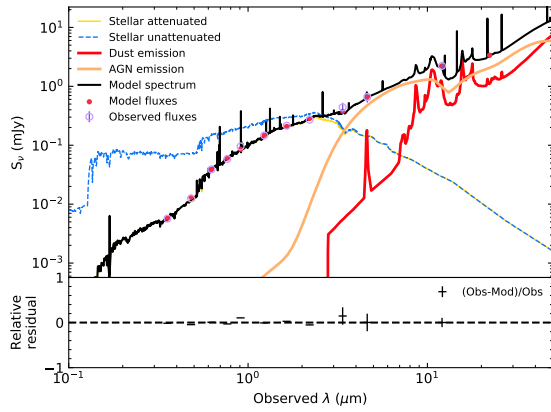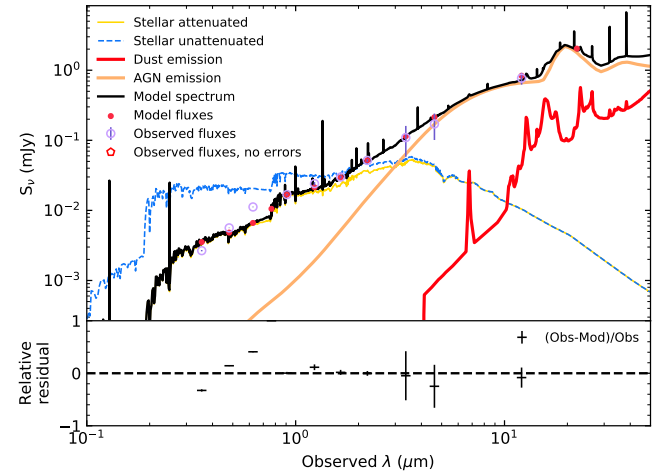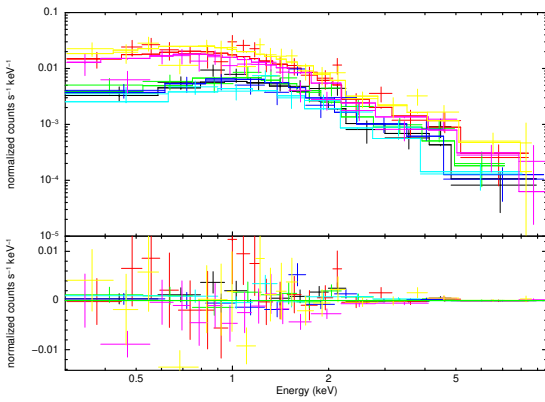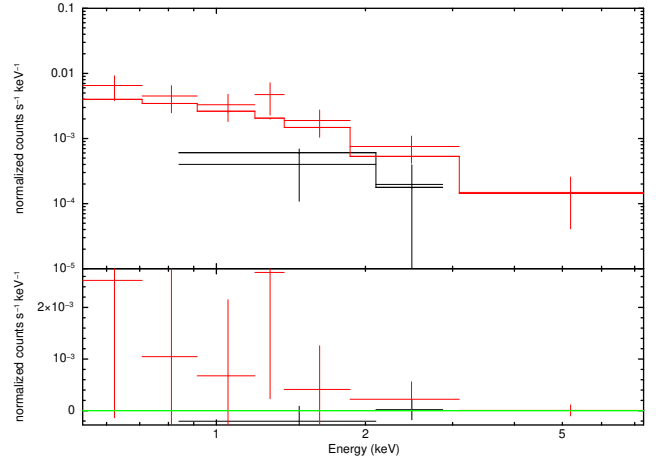
Fig. A.2. J022848.4−044426 (2,2,1), $z = 1.046$.
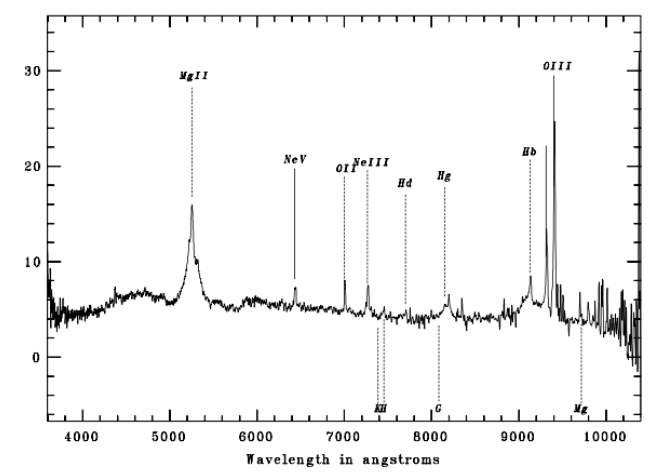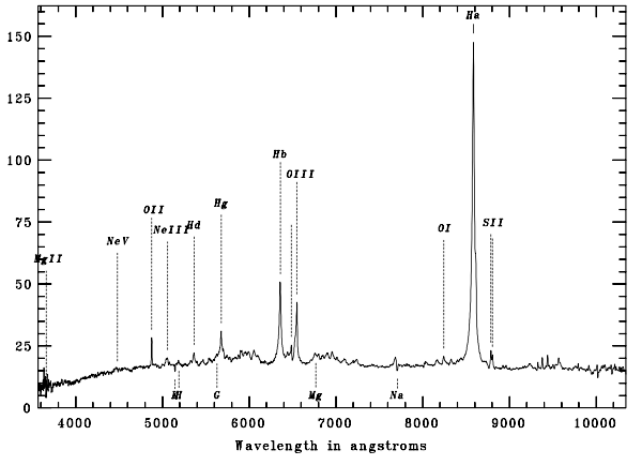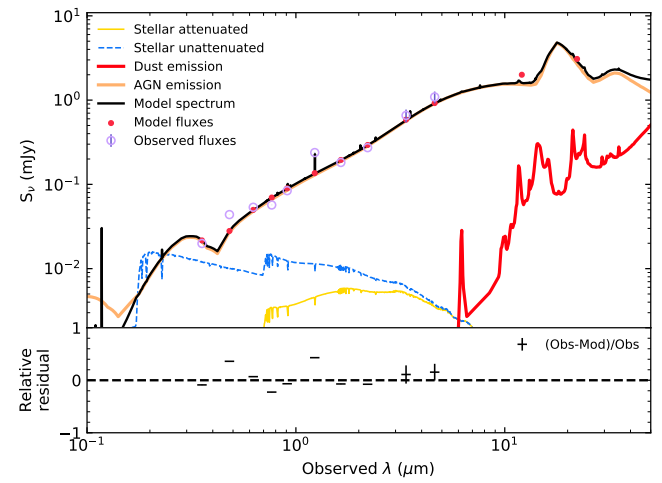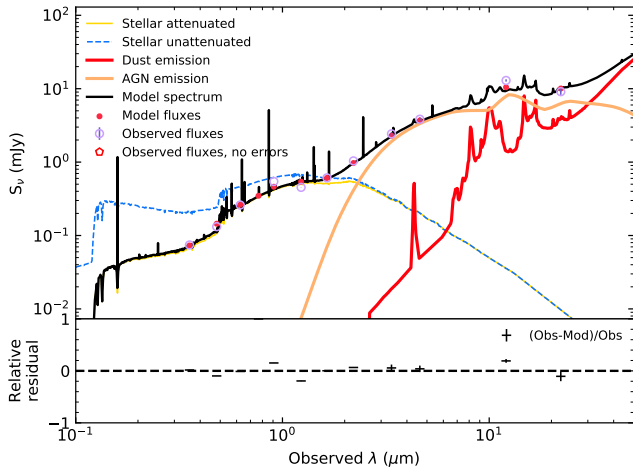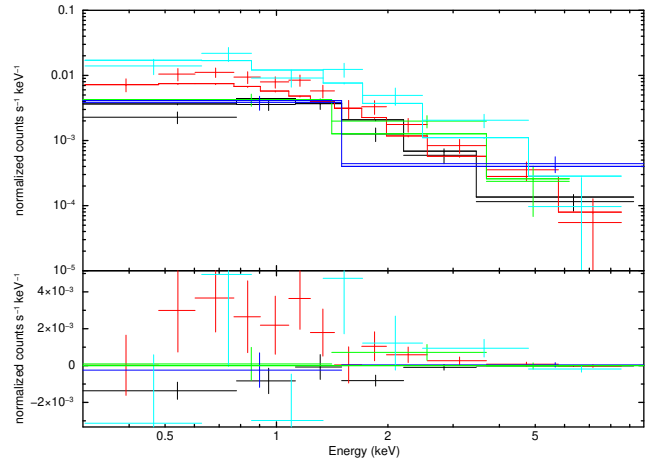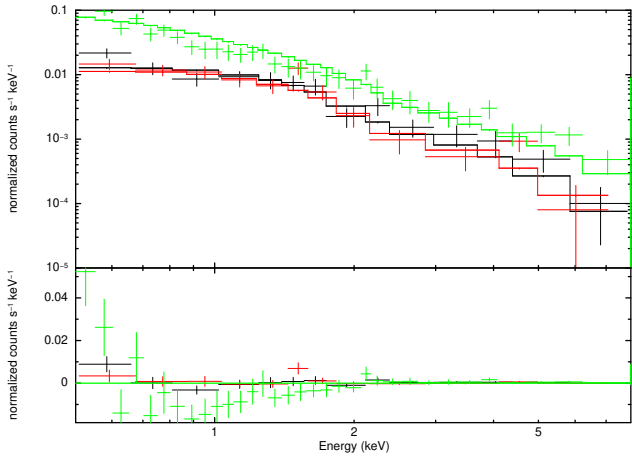
Fig. A.3. J022928.4−051124 (2,2,1), $z = 0.307$.

Fig. A.4. J022809.0−041235 (1,1,1), $z = 0.879$.
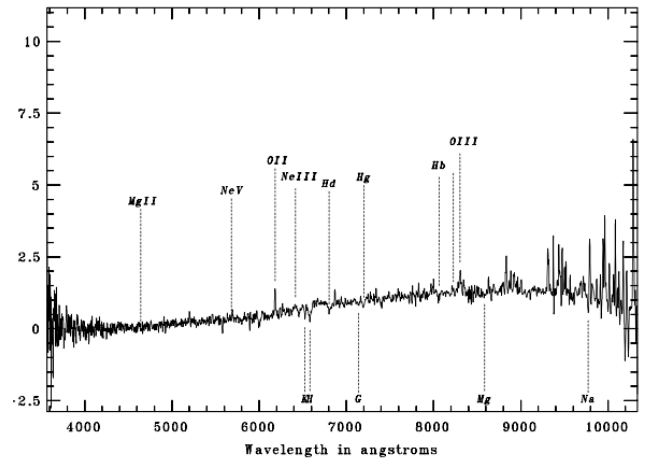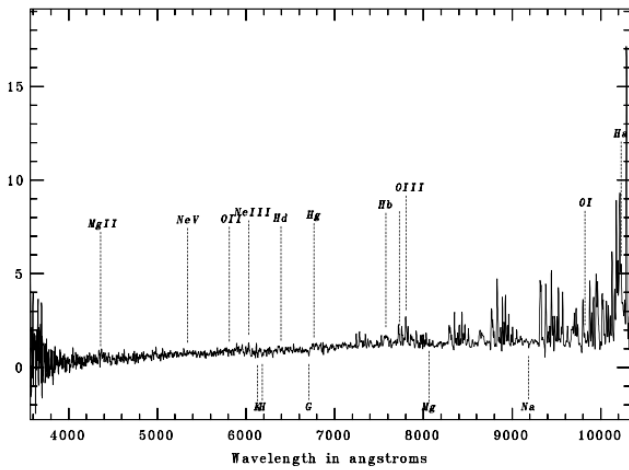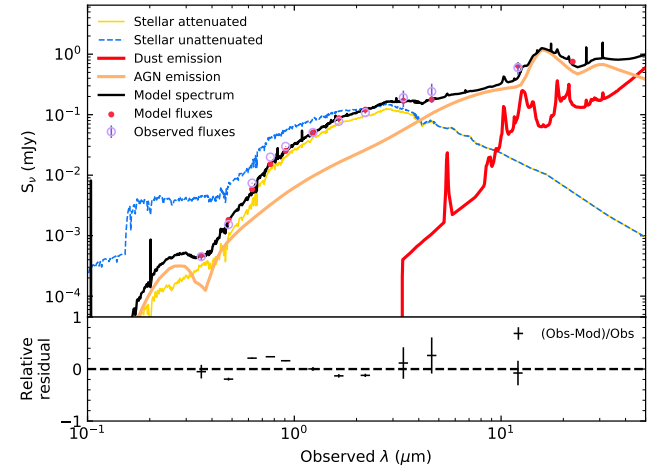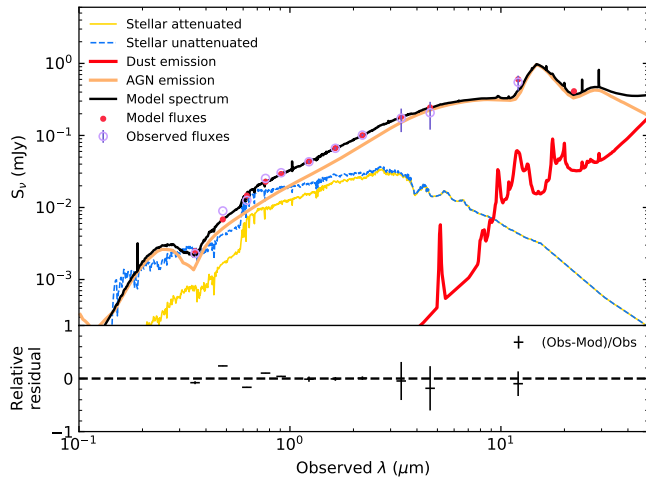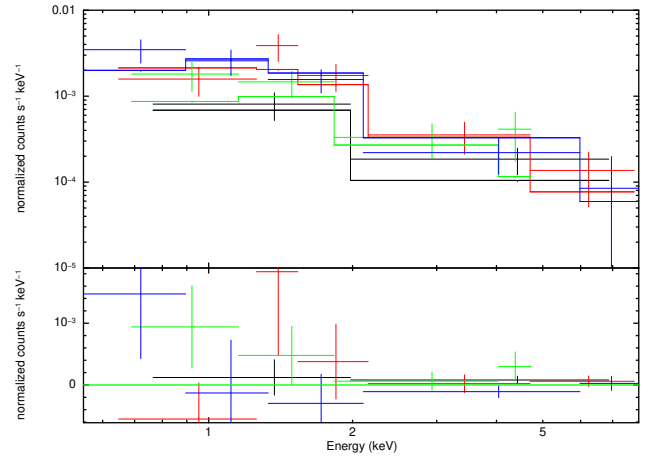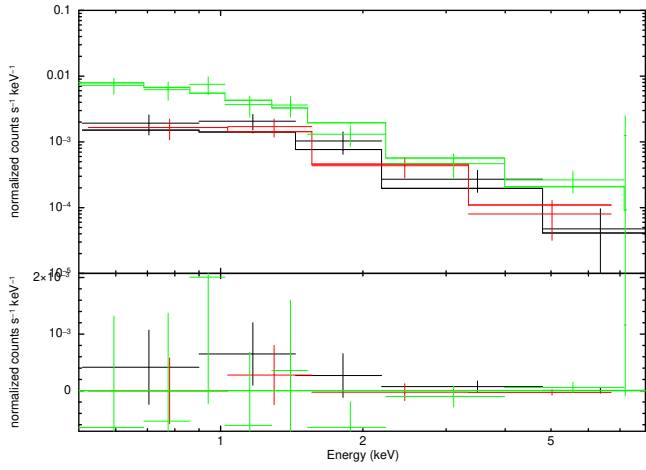
Fig. A.5. J020654.9−064552 (1,2,2), $z = 1.412$.

Fig. A.6. J020410.4−063924 (2,2,2), $z = 0.414$.
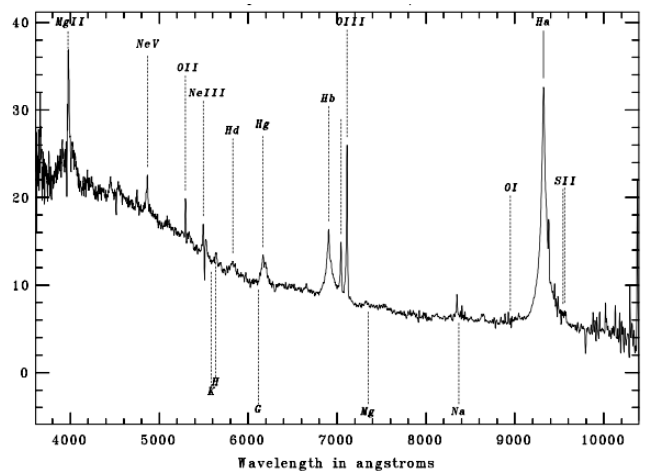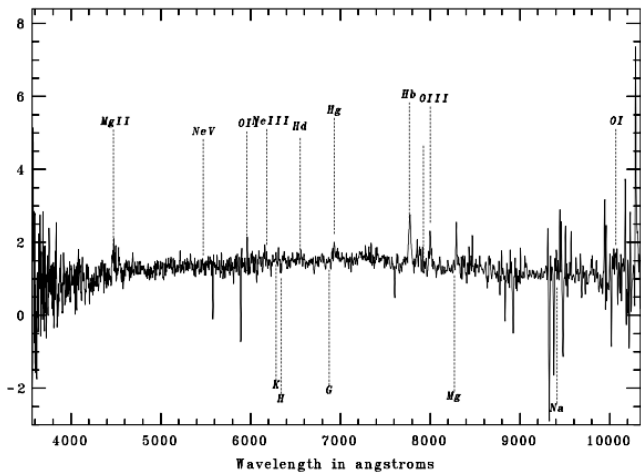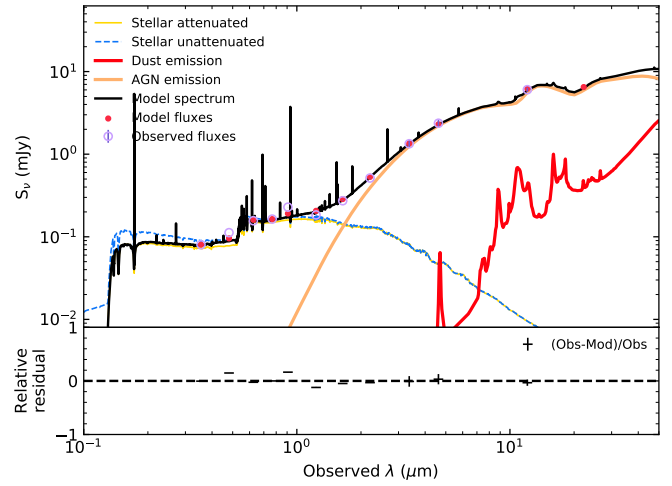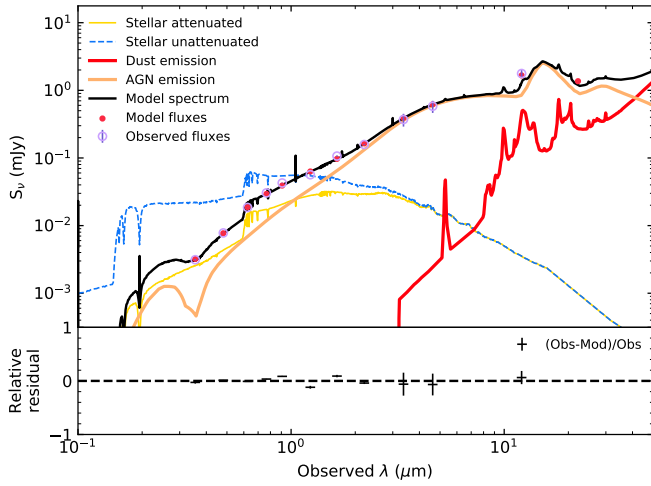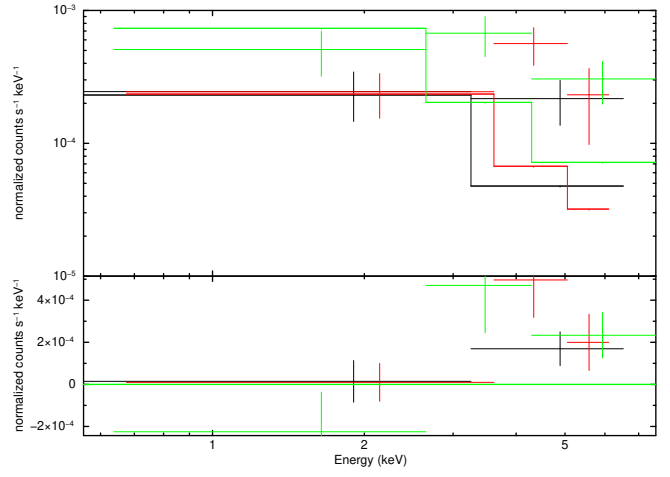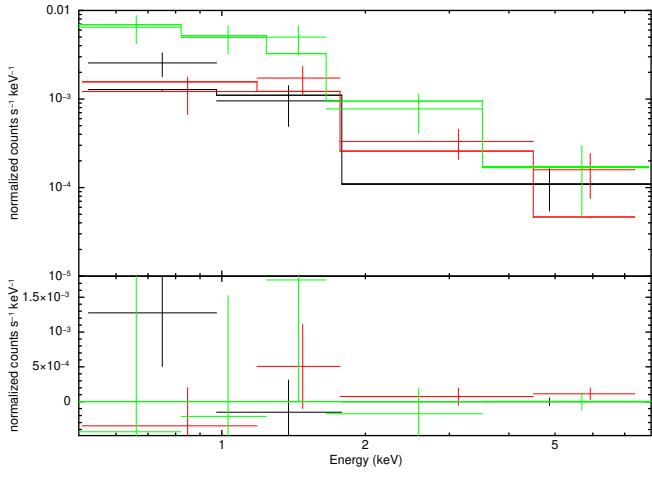
Fig. A.7. J023315.5−054747 (1,2,2), $z = 0.598$.

Fig. A.8. J021337.9−042814 (2,2,1), $z = 0.419$.
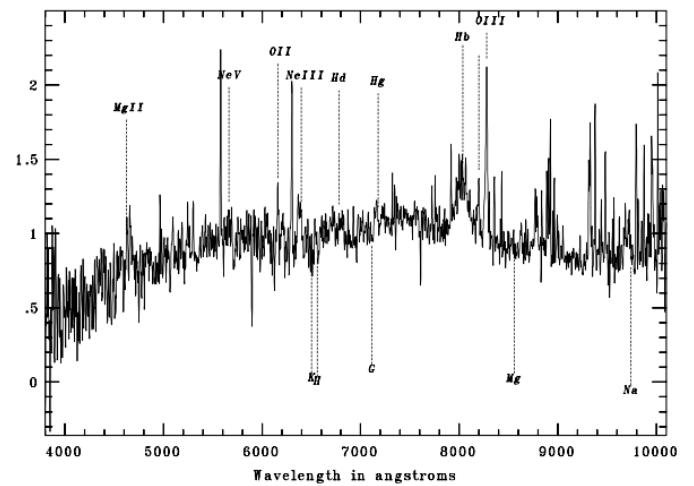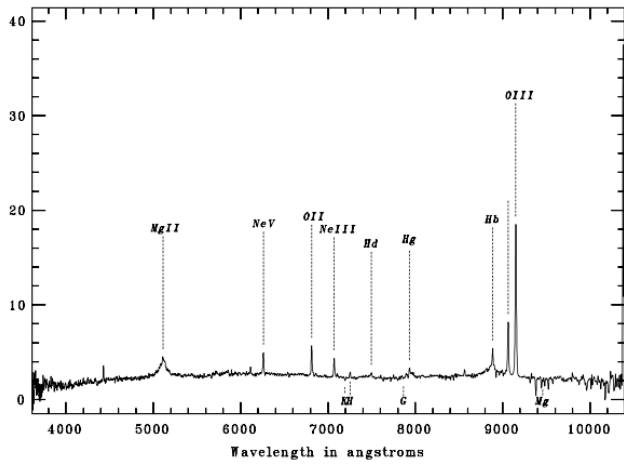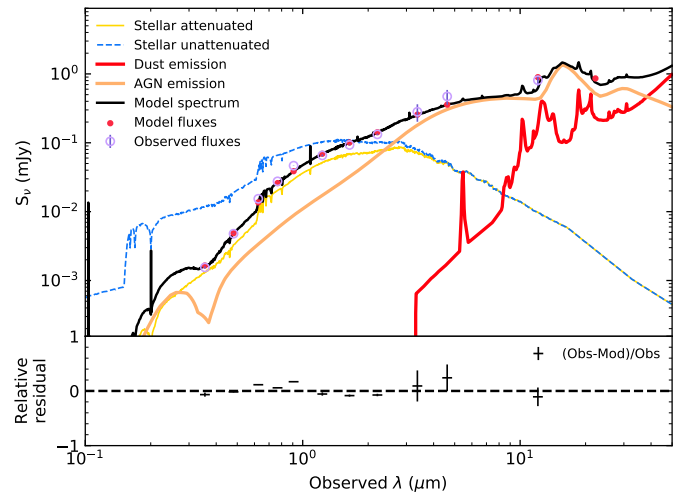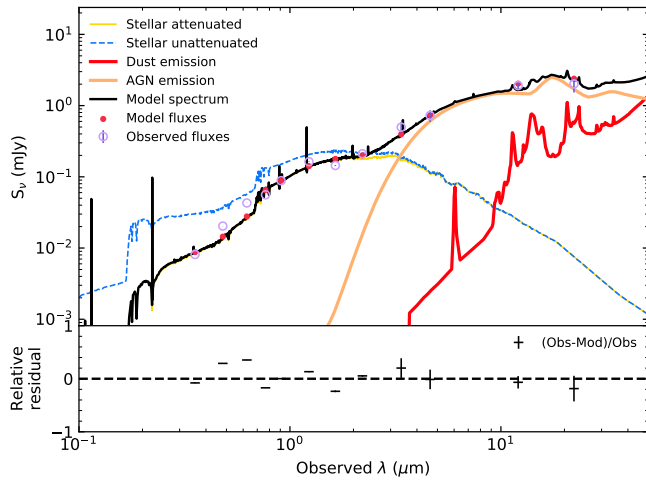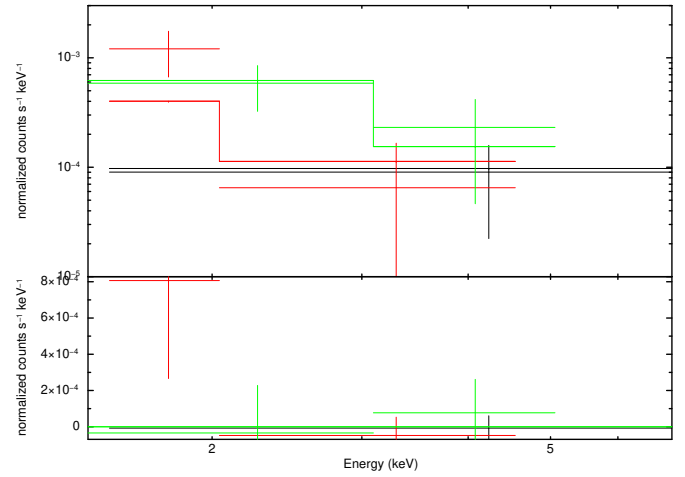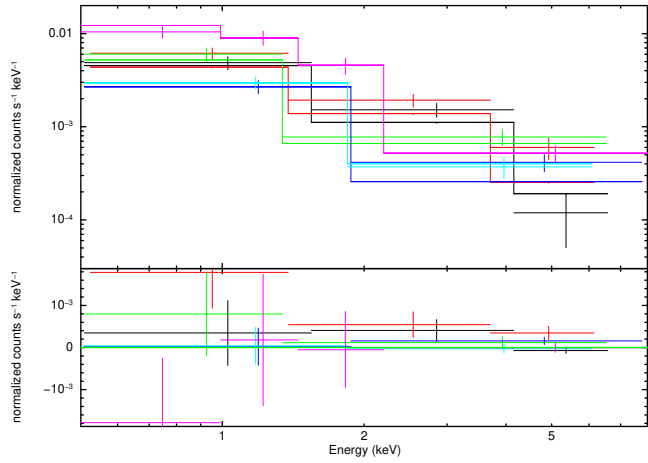
Fig. A.9. J020436.4−042833 (1,2,1), $z = 0.827$.

Fig. A.10. J020543.0−051656 (2,2,1), $z = 0.653$.
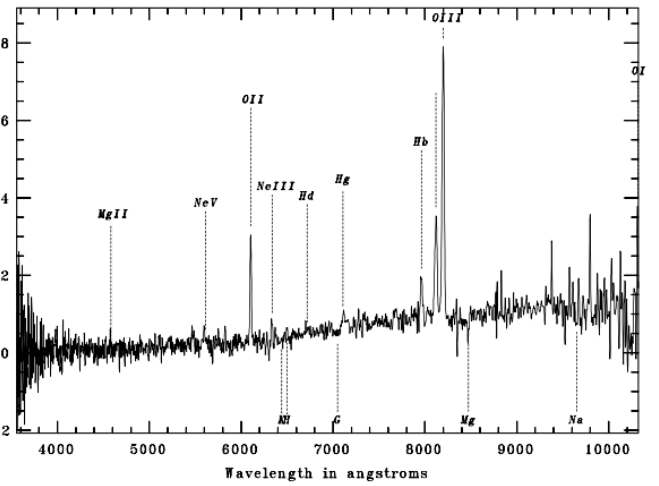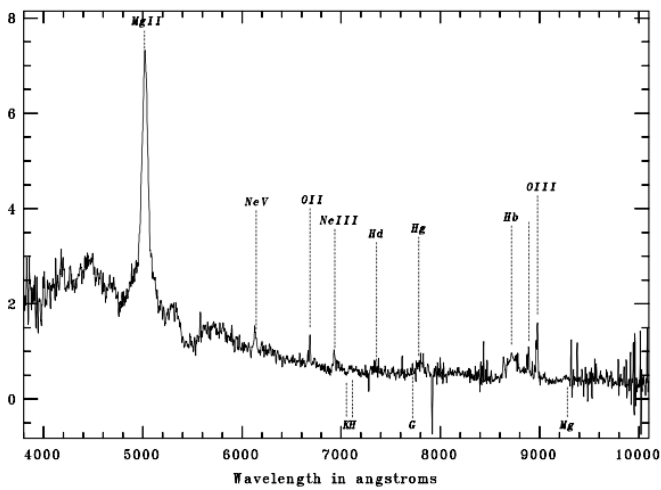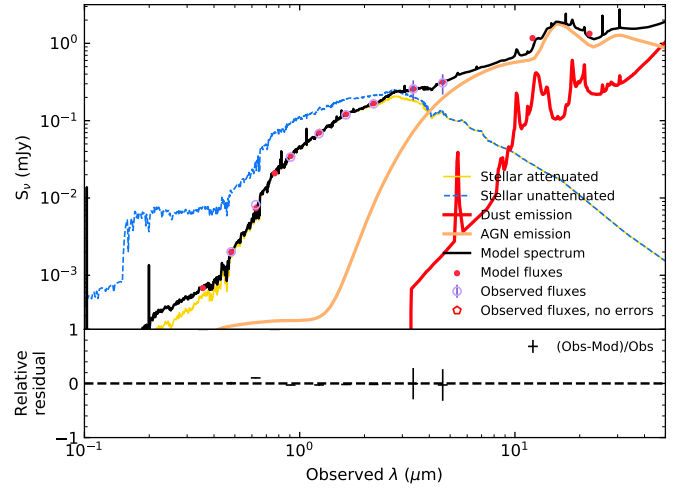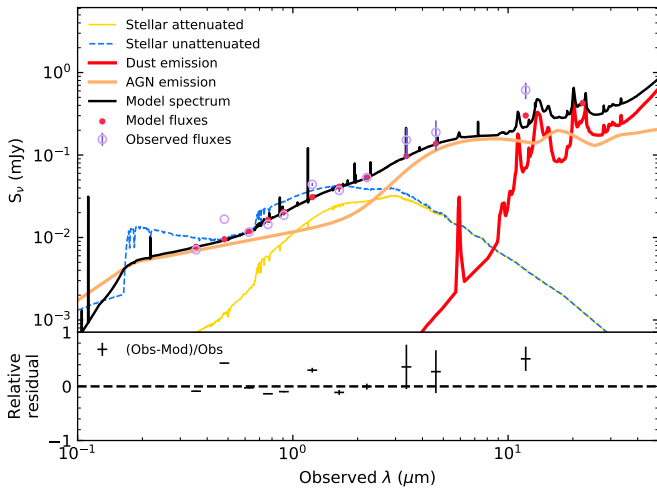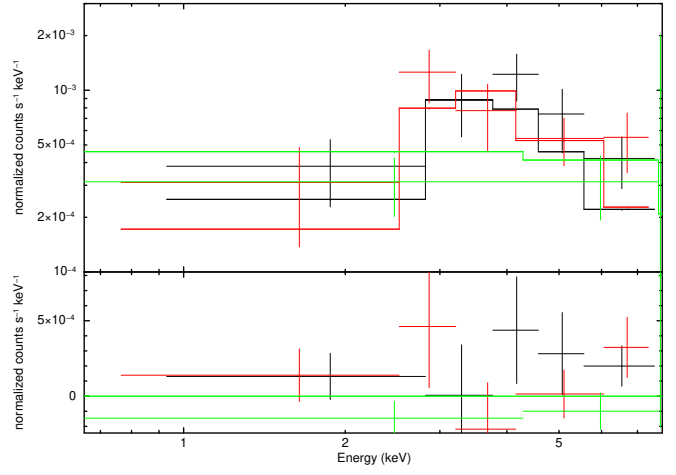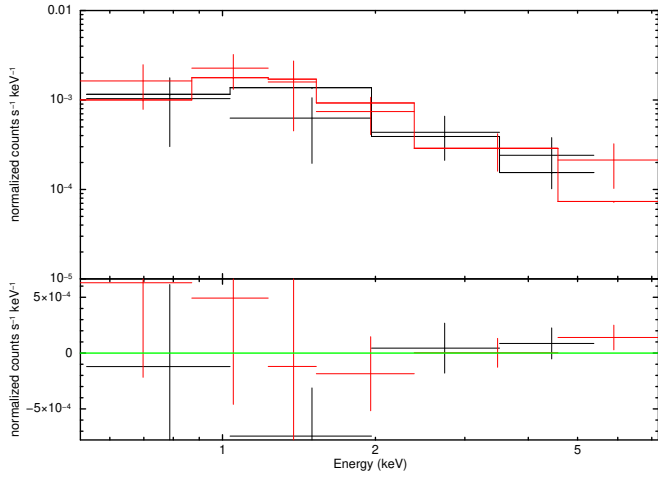
Fig. A.11. J020517.3−051024 (2,0,1), $z = 0.792$.

Fig. A.12. J022244.3−030525 (2,2,2), $z = 0.637$.
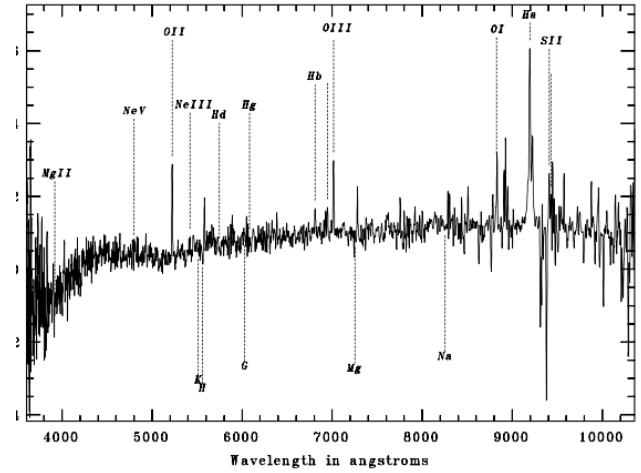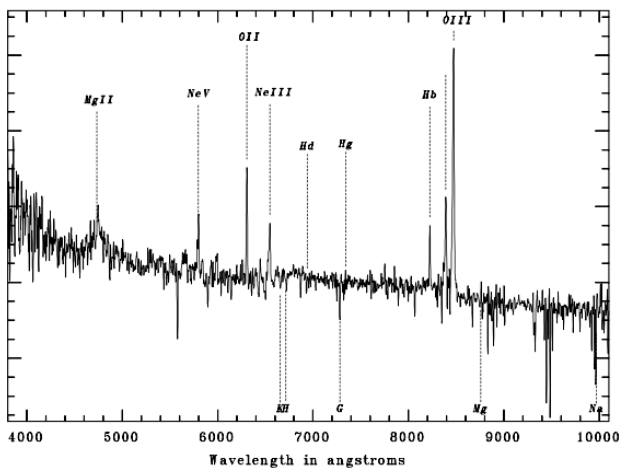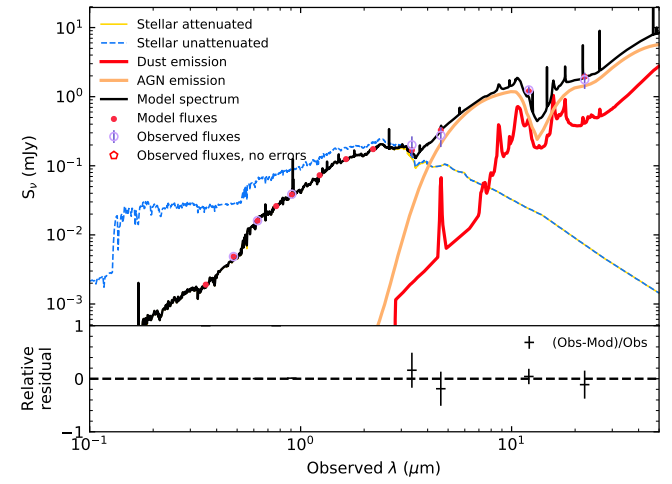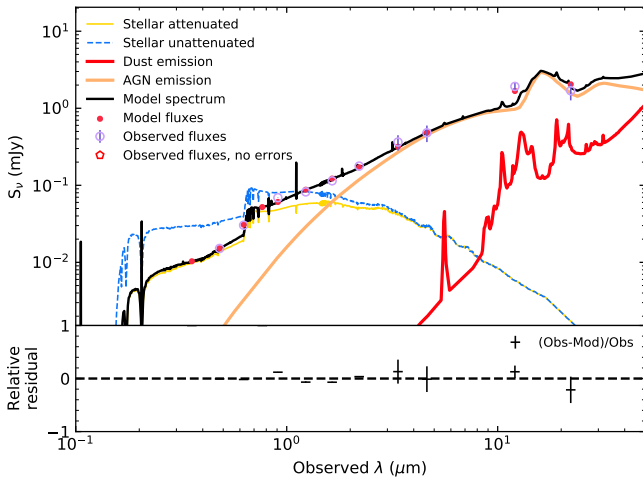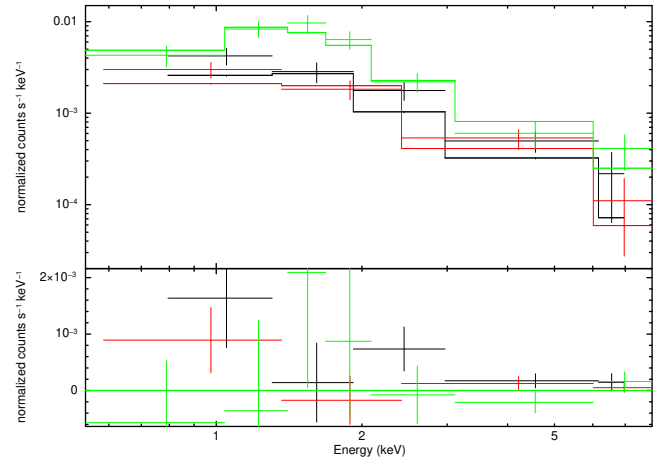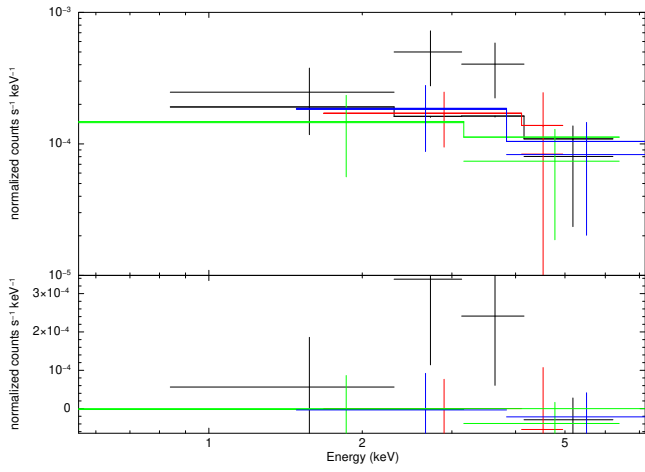
Fig. A.13. J022323.4−031157 (2,2,3), $z = 0.691$.

Fig. A.14. J022209.6−025023 (2,2,2), $z = 0.400$.
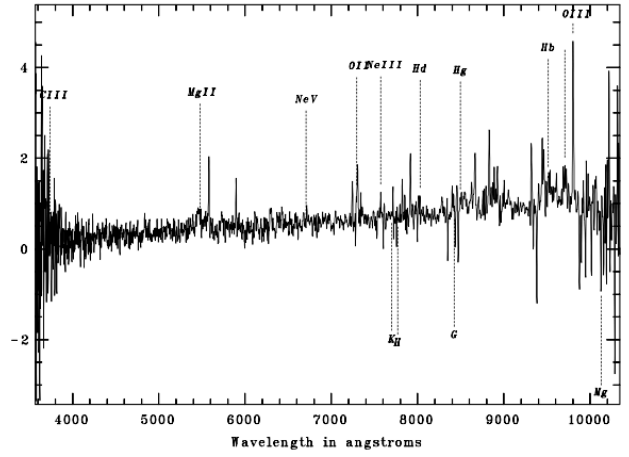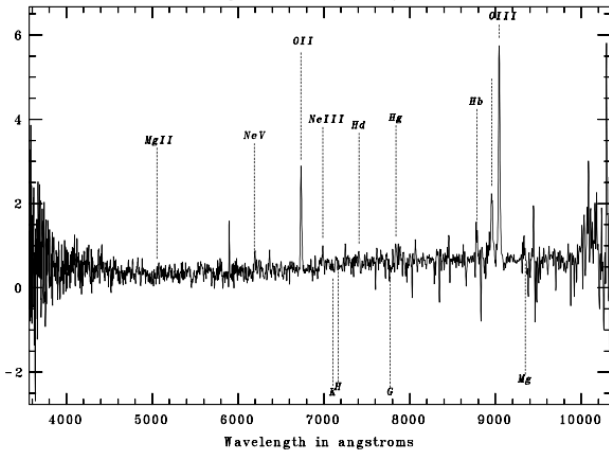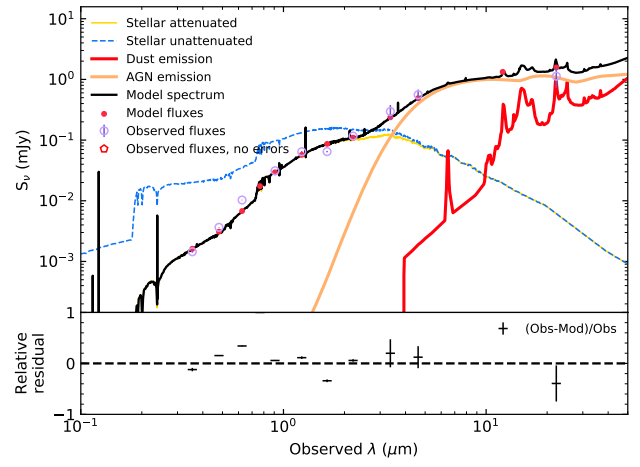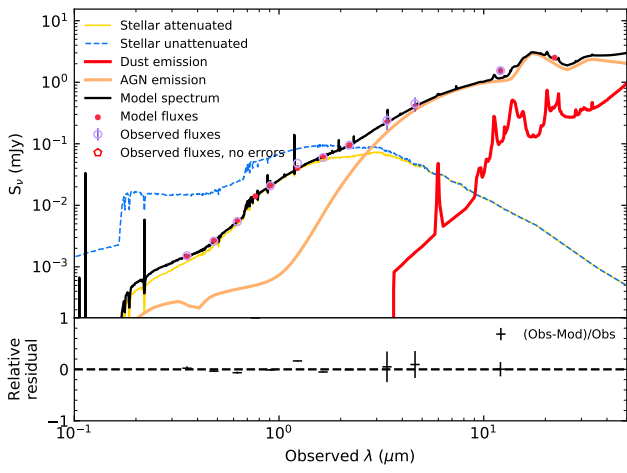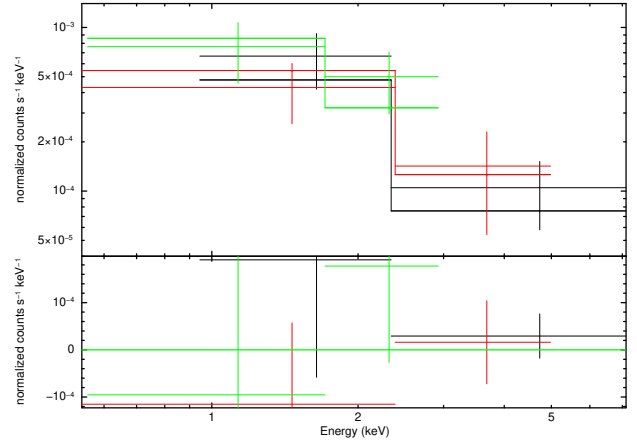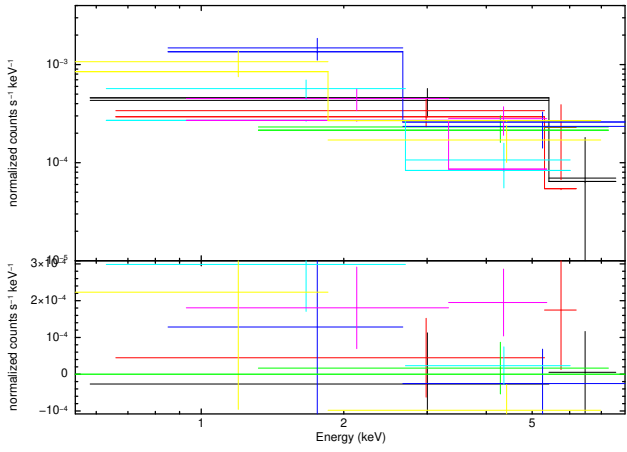
Fig. A.15. J022750.7−052232 (2,2,3), $z = 0.804$.

Fig. A.16. J022758.4−053306 (1,2,2), $z = 0.956$.
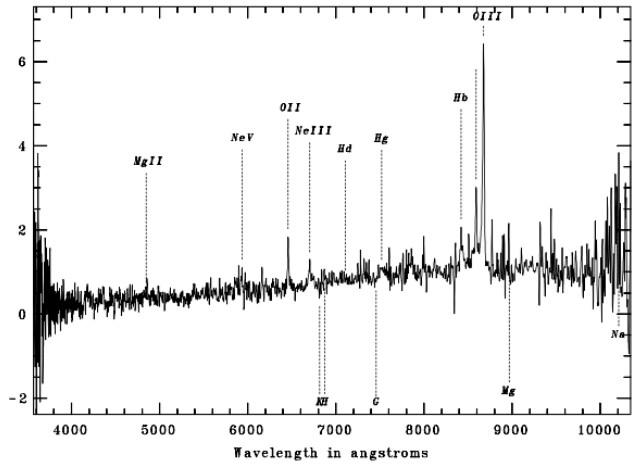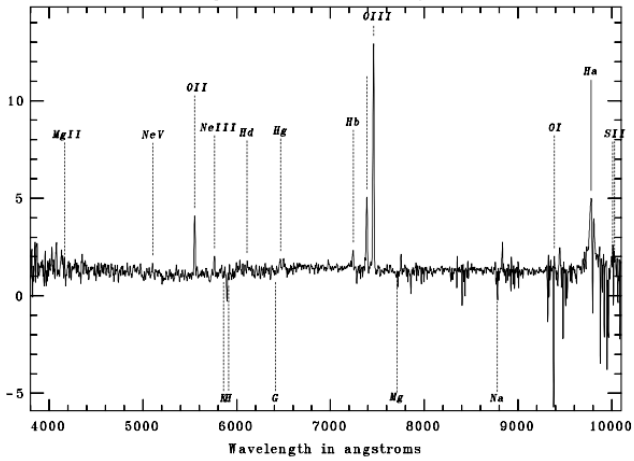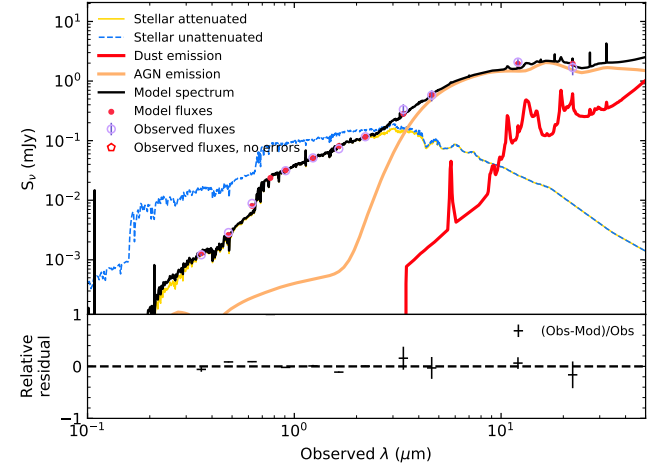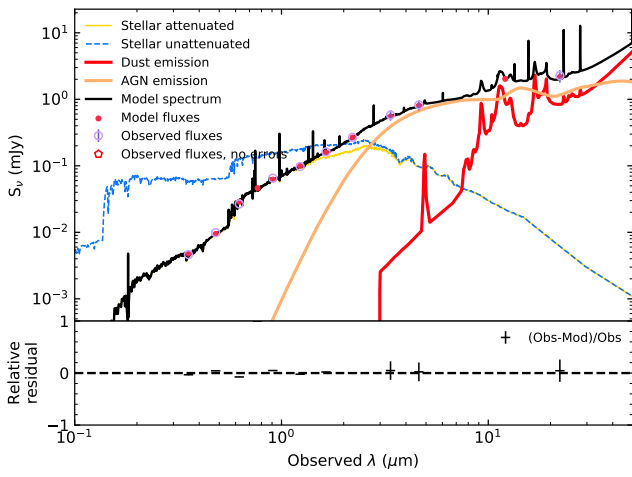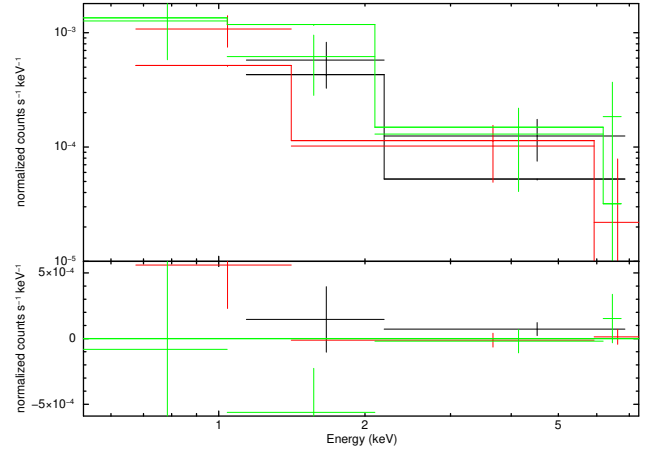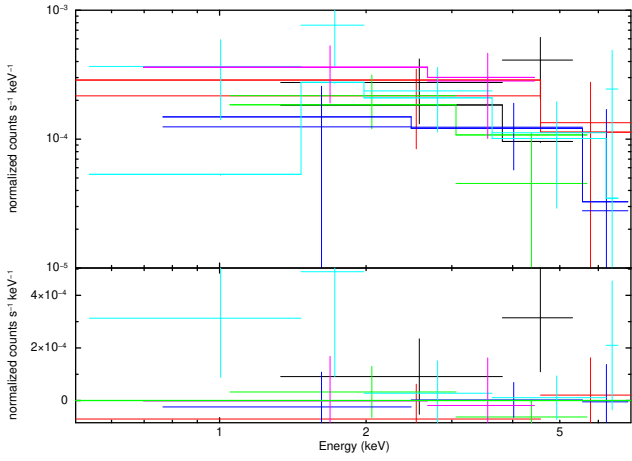
Fig. A.17. J022453.2−054050 (2,2,3), $z = 0.488$.

Fig. A.18. J022258.8−055757 (1,2,3), $z = 0.732$.
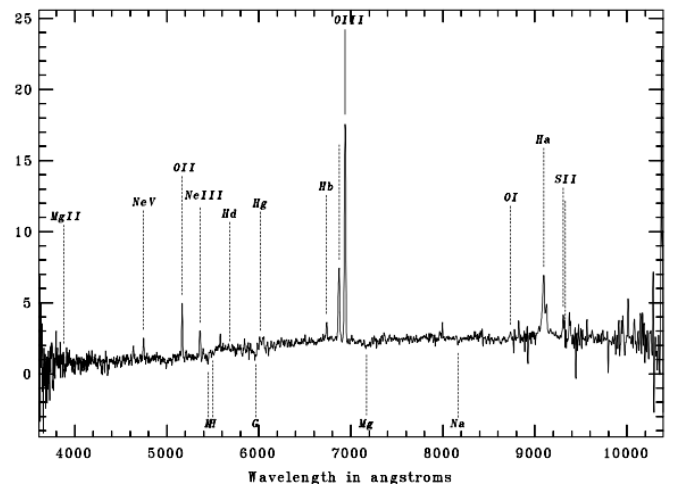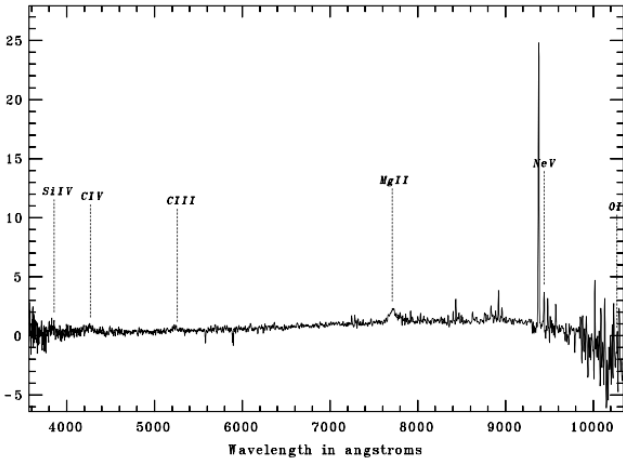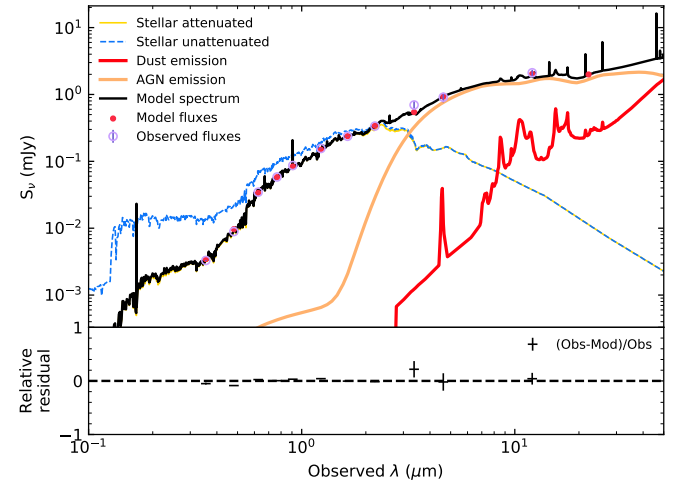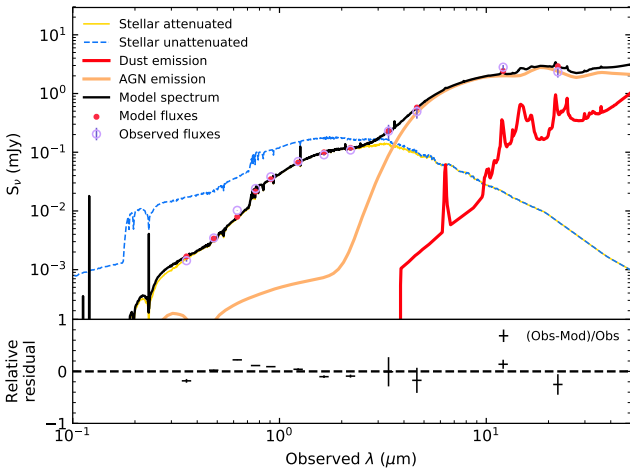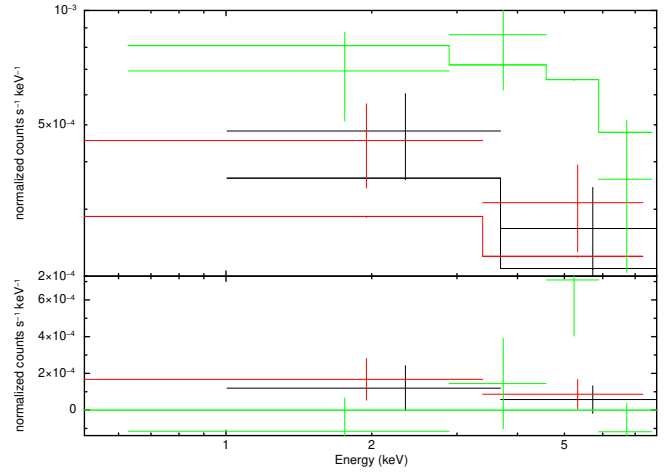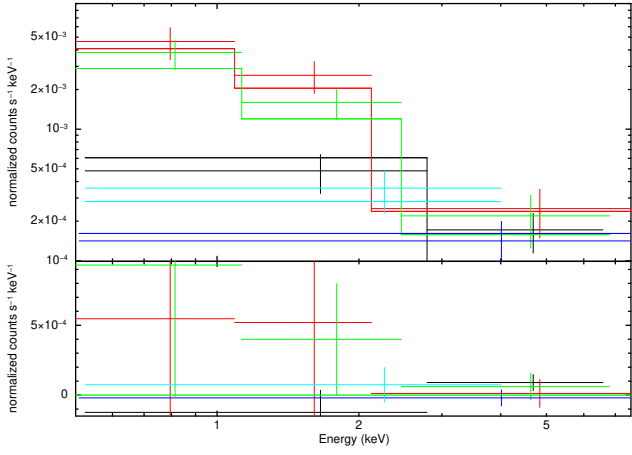
Fig. A.19. J021844.6−054054 (1,2,3), $z = 0.671$.

Fig. A.20. J021523.2−044337 (1,2,2), $z = 0.860$.
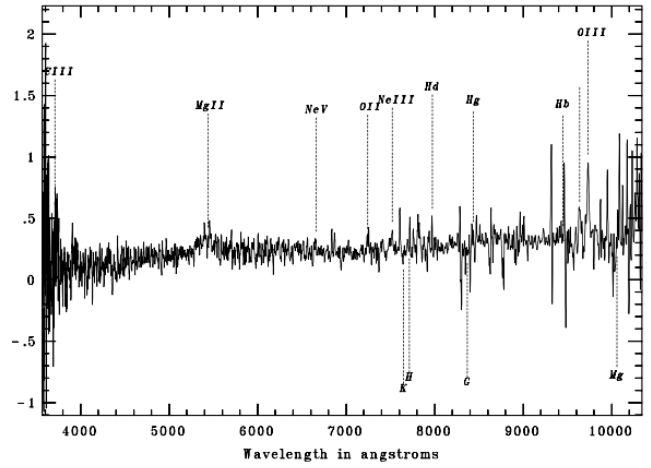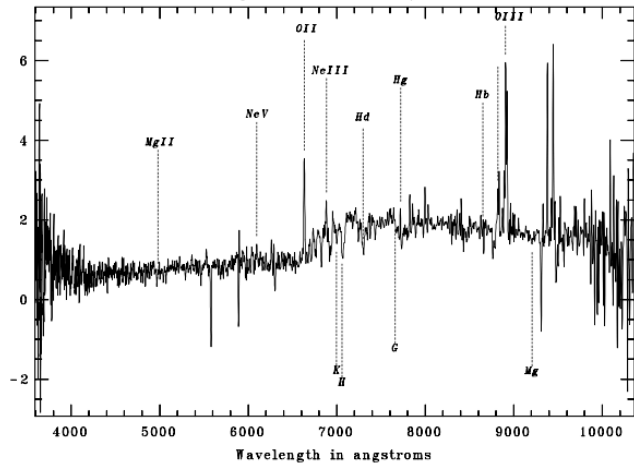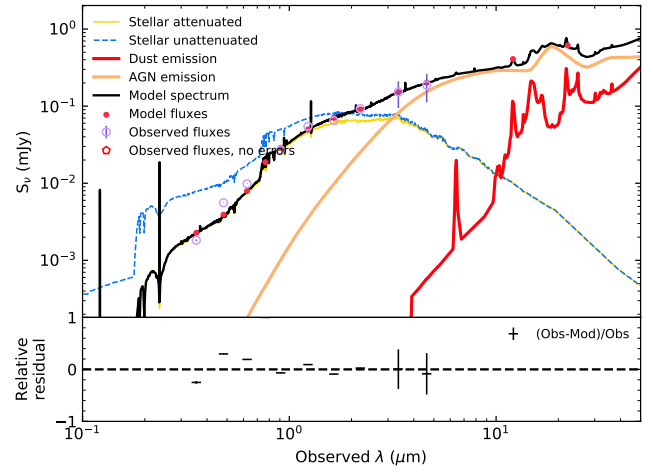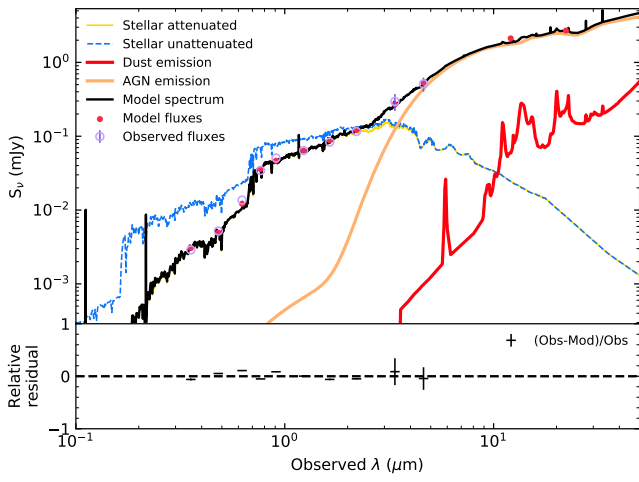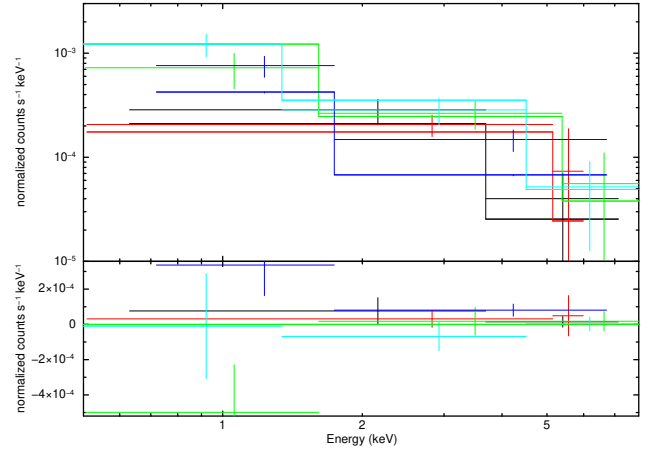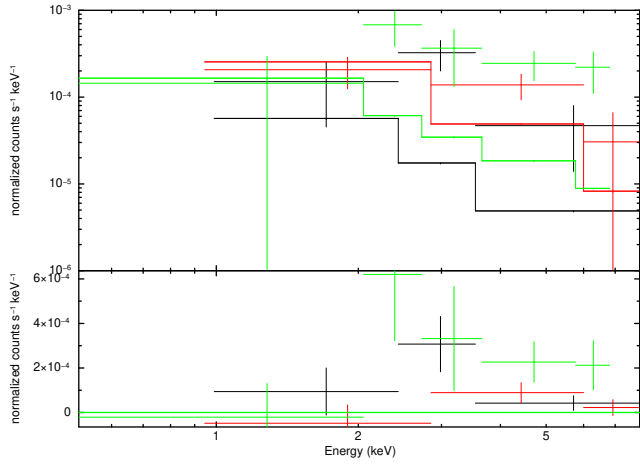
Fig. A.21. J022321.9−045739 (2,2,2), $z = 0.779$.

Fig. A.22. J022443.6−050905 (2,2,3), $z = 0.943$.
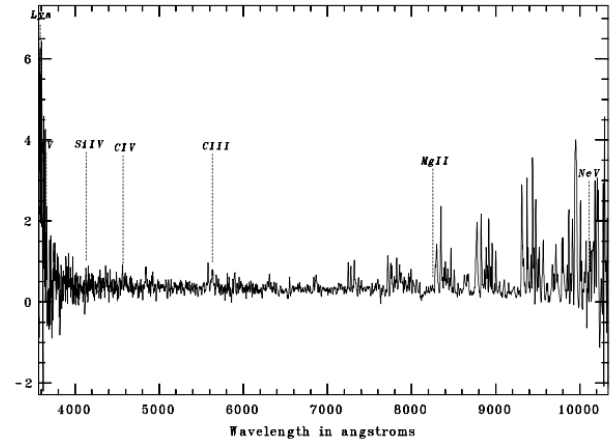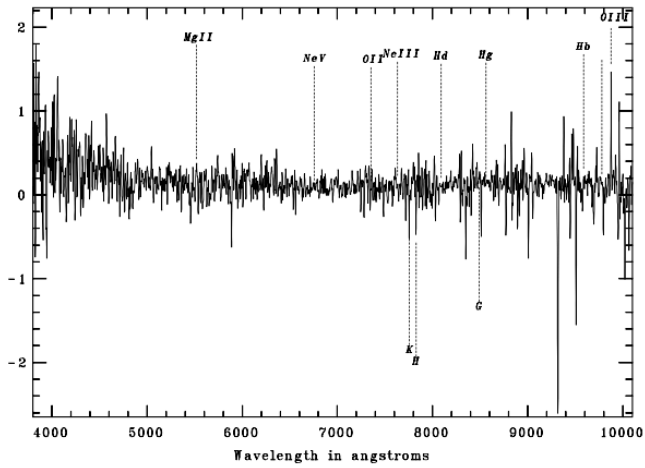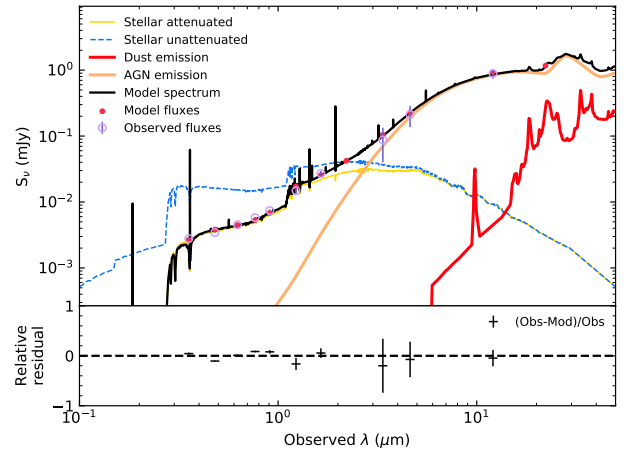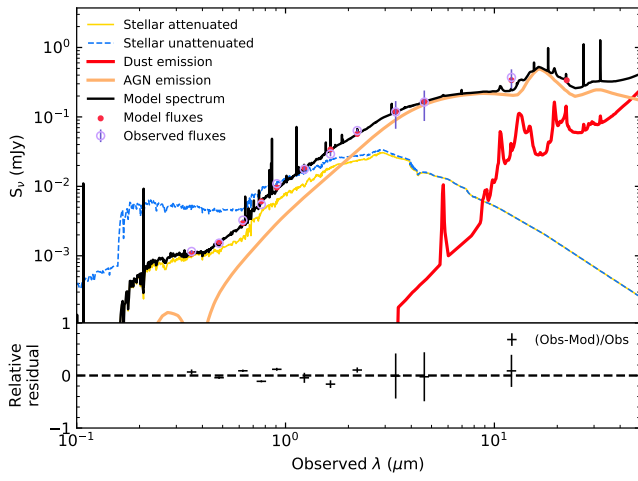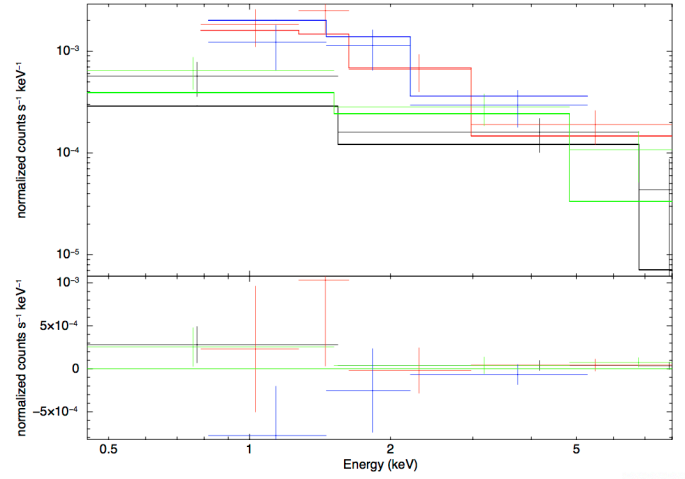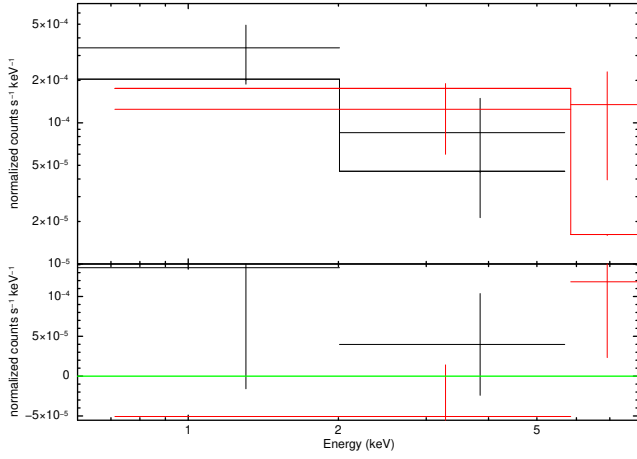
Fig. A.23. J023418.0−041833 (1,2,0), $z = 0.582$.

Fig. A.24. J020543.7−063807 (1,2,0), $z = 0.772$.
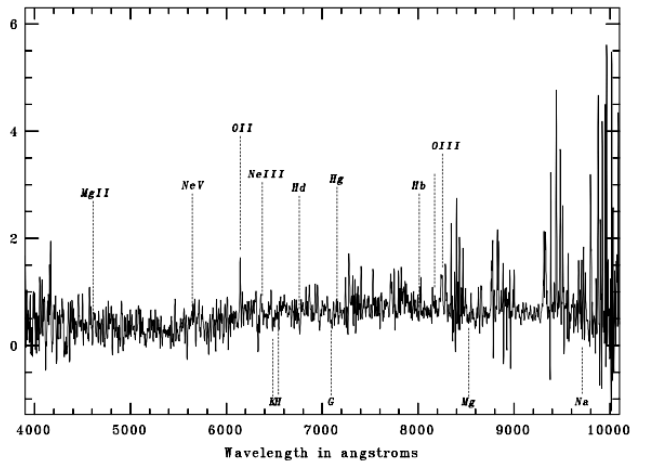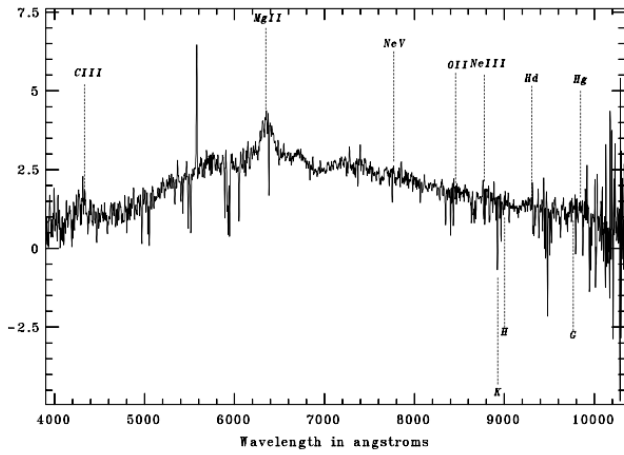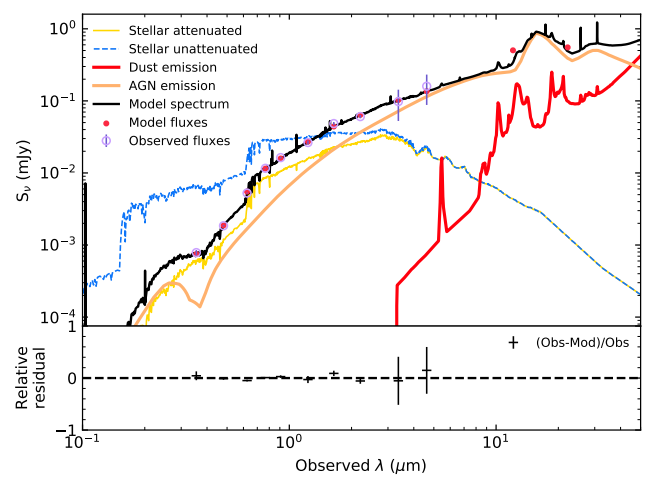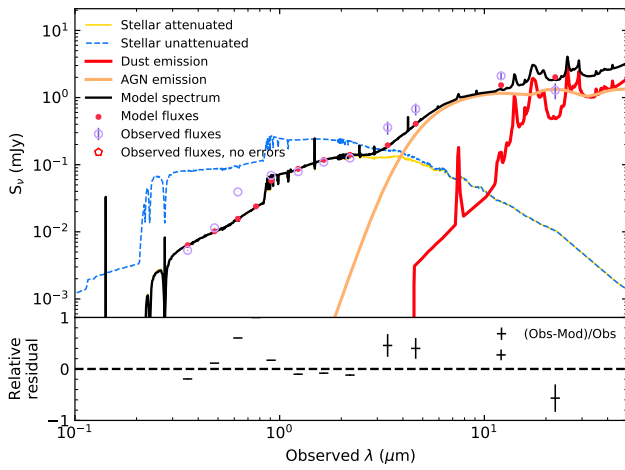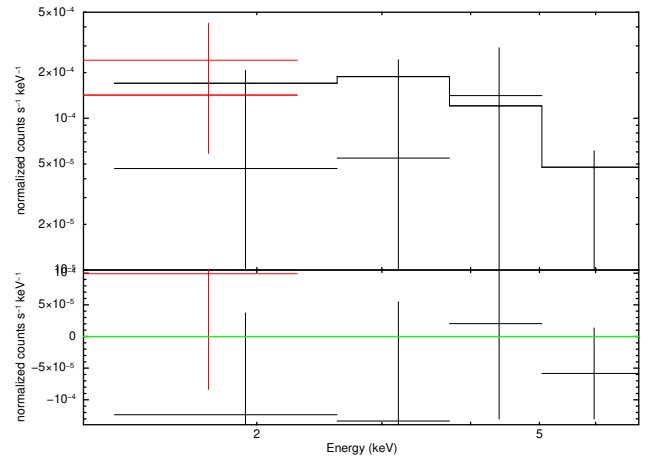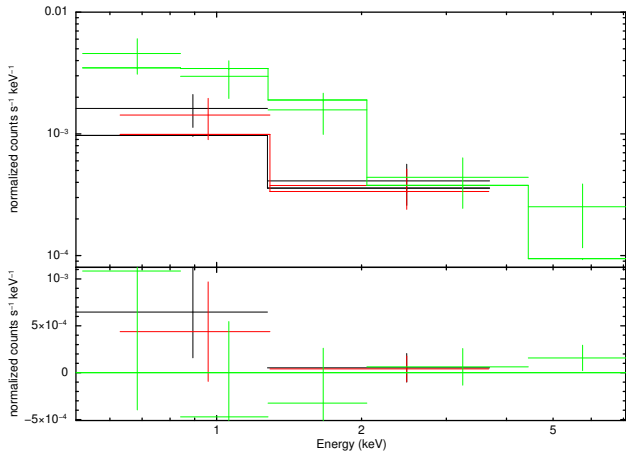
Fig. A.25. J022932.6−055438 (1,2,1), $z = 1.263$.

Fig. A.26. J021239.2−054816 (2,2,0), $z = 0.711$.

Fig. A.27. J021511.4−060805 (2,2,1), $z = 0.772$.
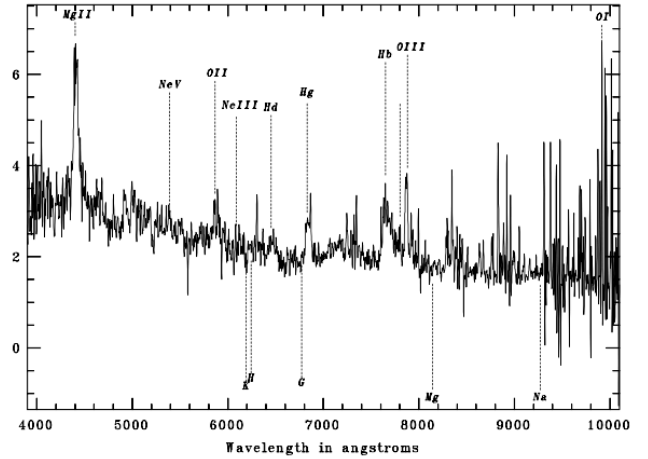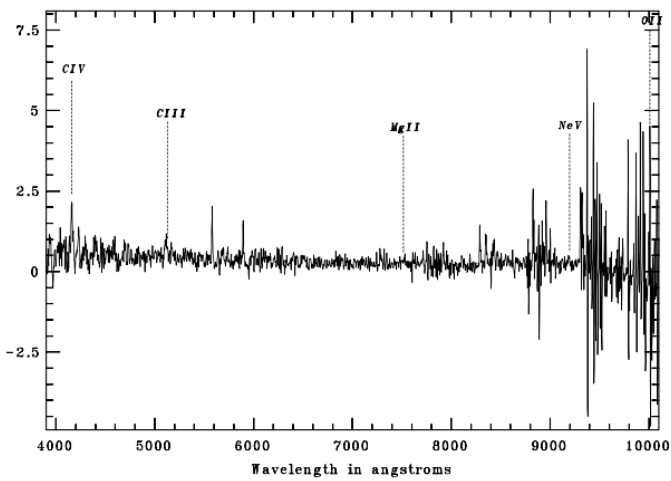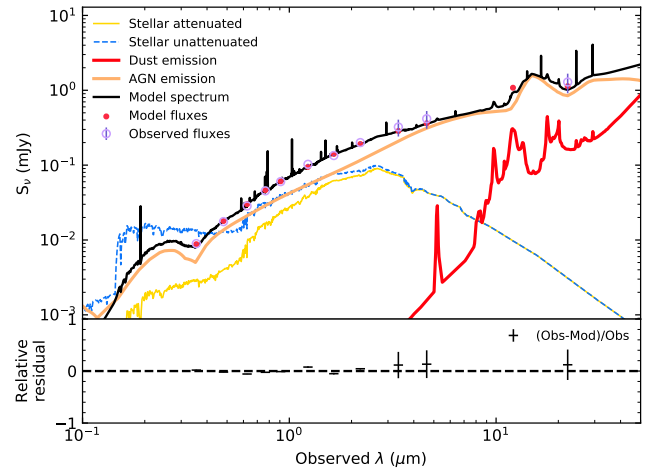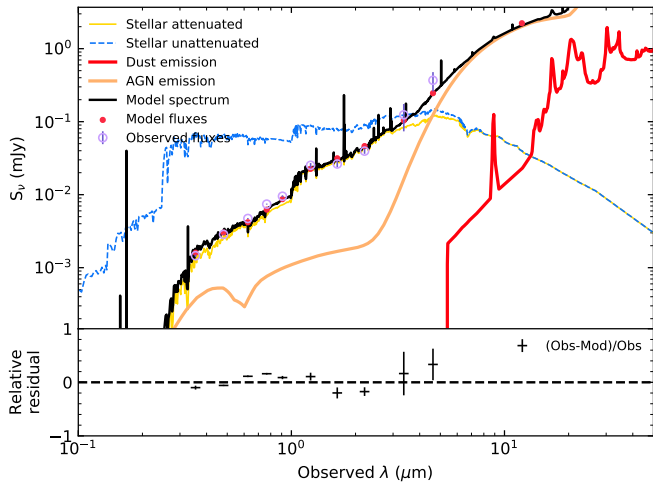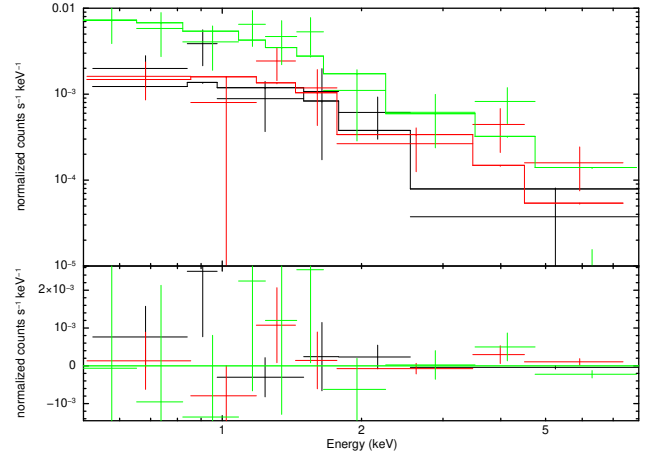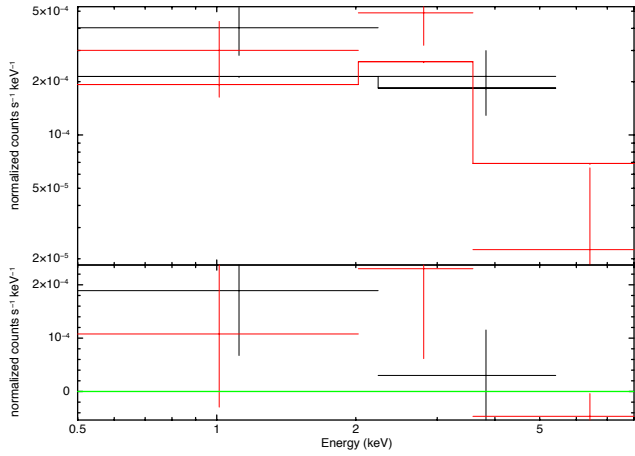
Fig. A.28. J021808.8−055630 (1,0,1), $z = 0.572$.
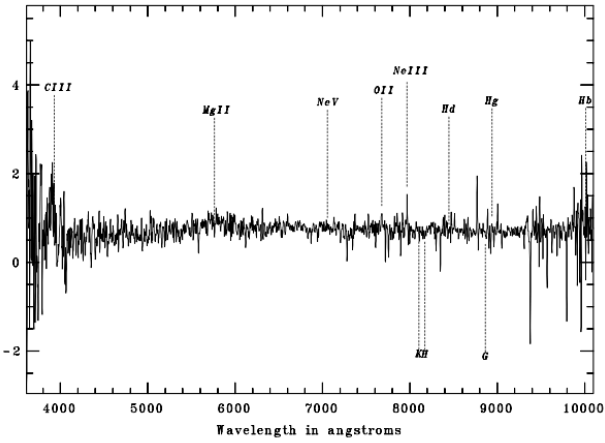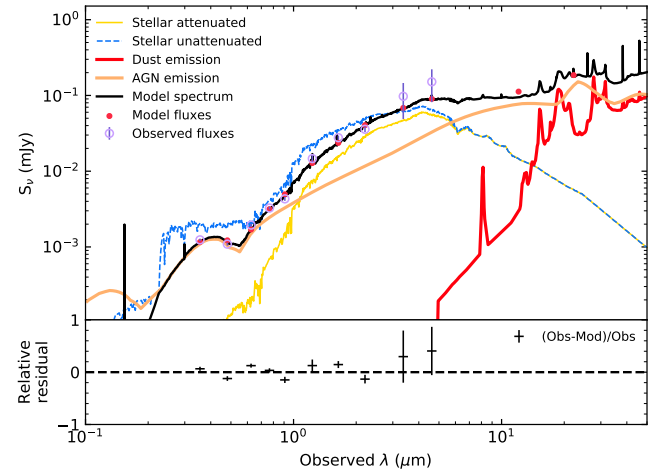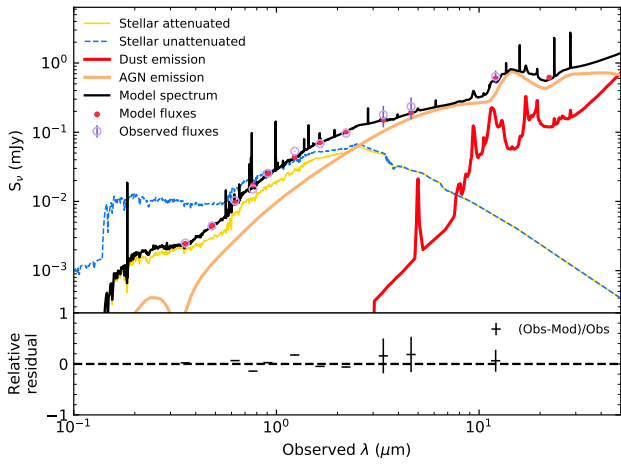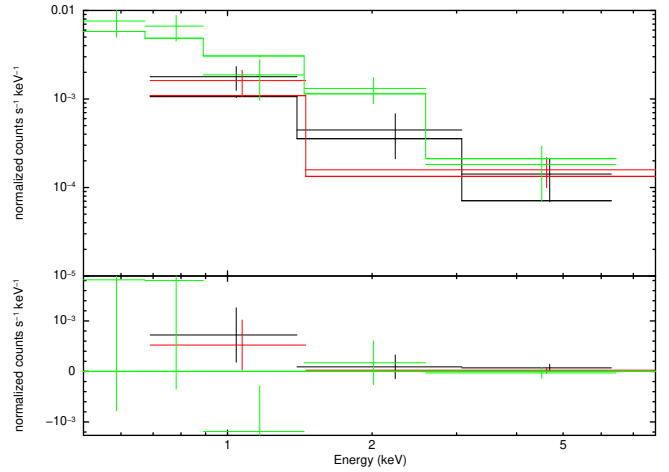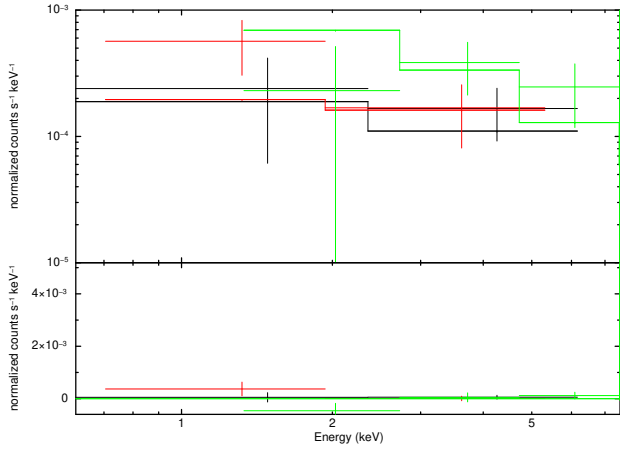
Fig. A.30. J020845.1−051354 (2,2), $z = 1.46$.

Fig. A.29. J022538.9−040821 (2,2,1), $z = 0.733$.
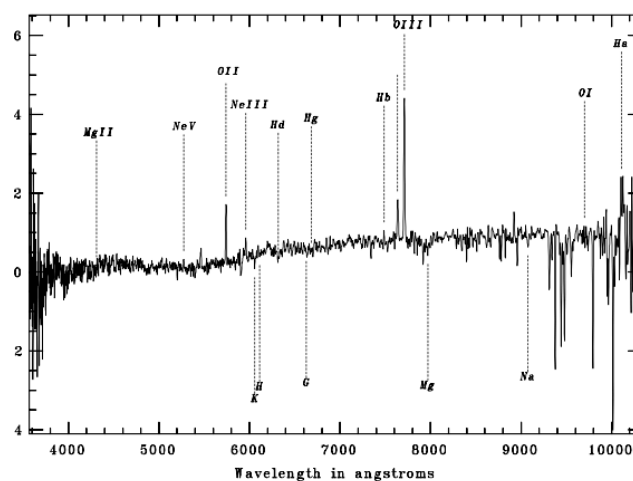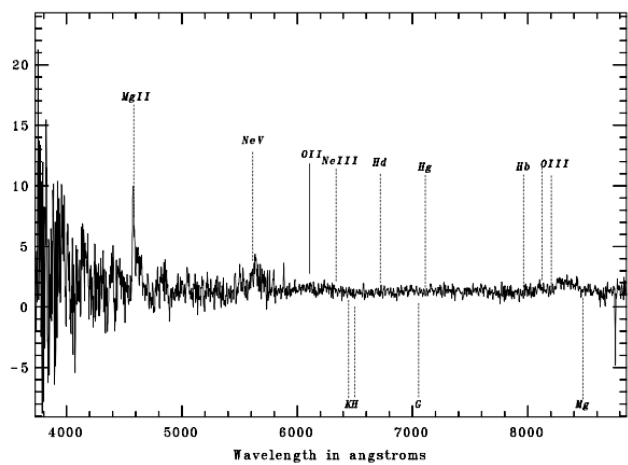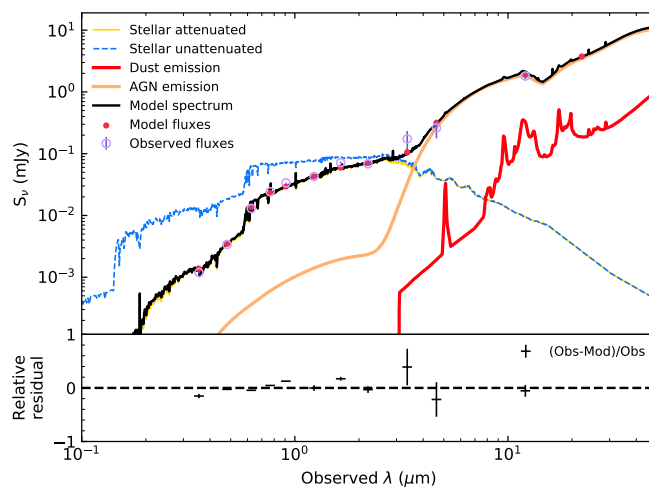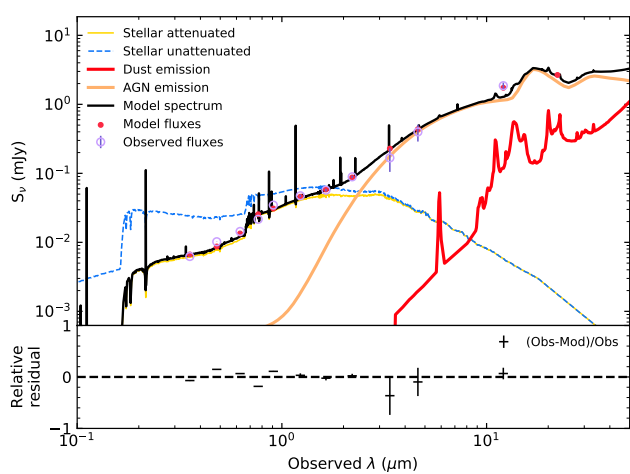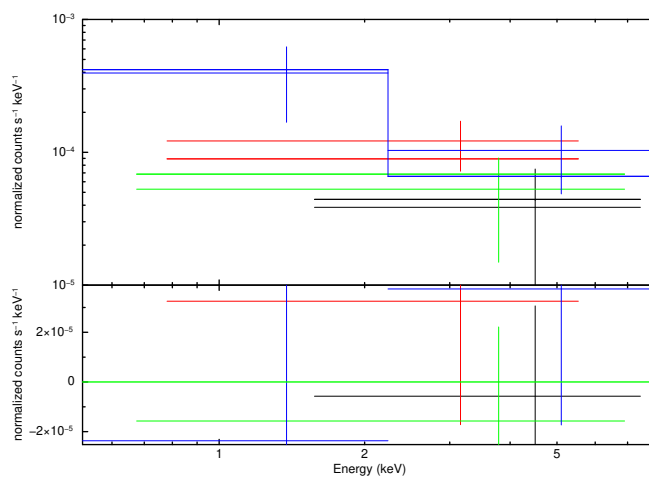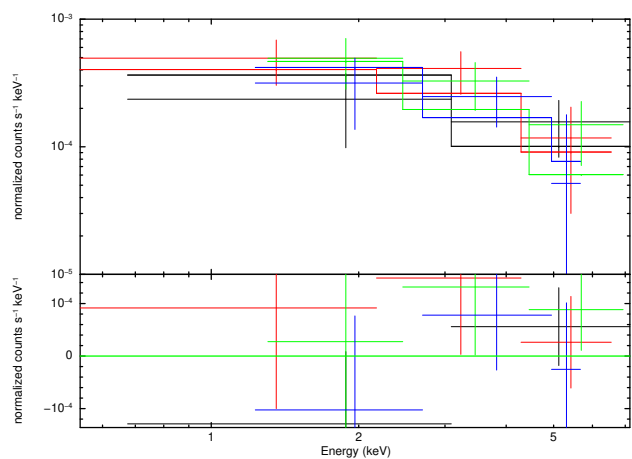
Fig. A.31. J020953.9−055102 (2,2,1), $z = 0.642$.

Fig. A.32. J020806.6−055739 (2,2,2), $z = 0.539$.
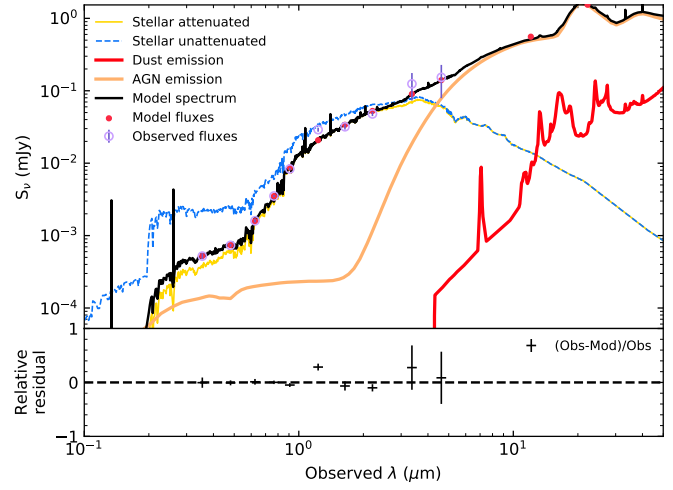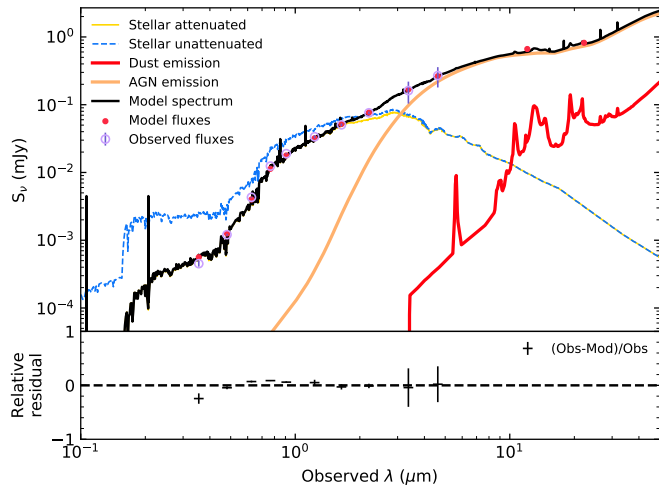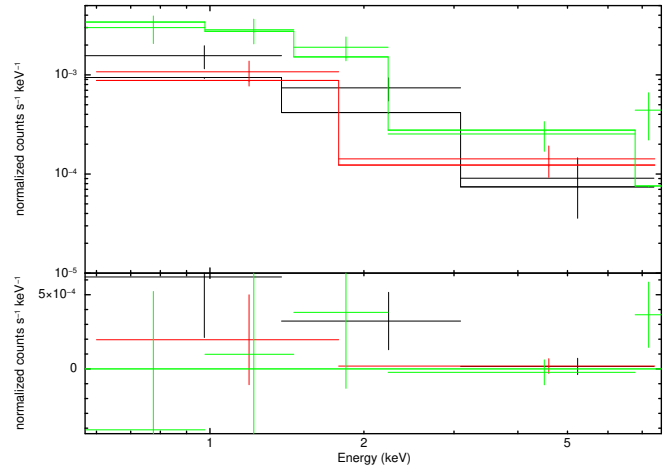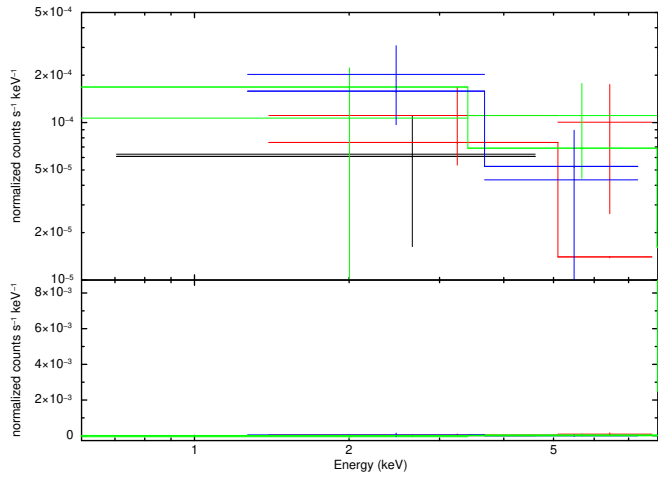
Fig. A.33. J021509.0−054305 (2,2), $z = 0.70$.

Fig. A.34. J021512.9−060558 (2,2), $z = 1.14$.
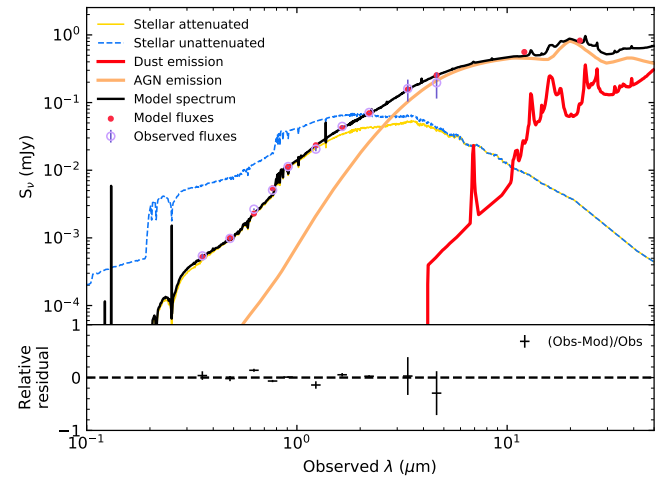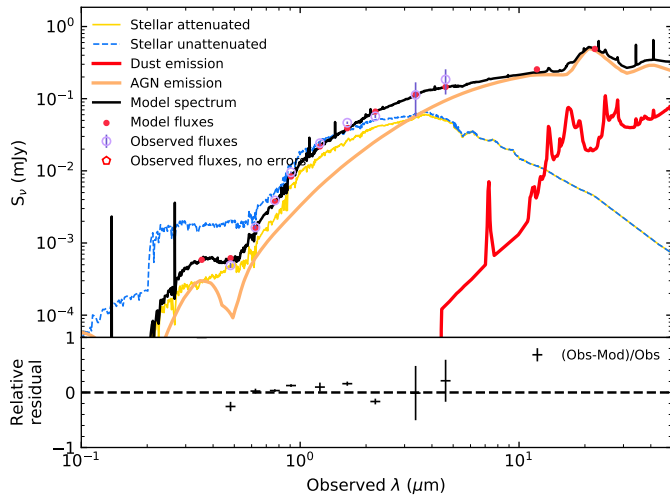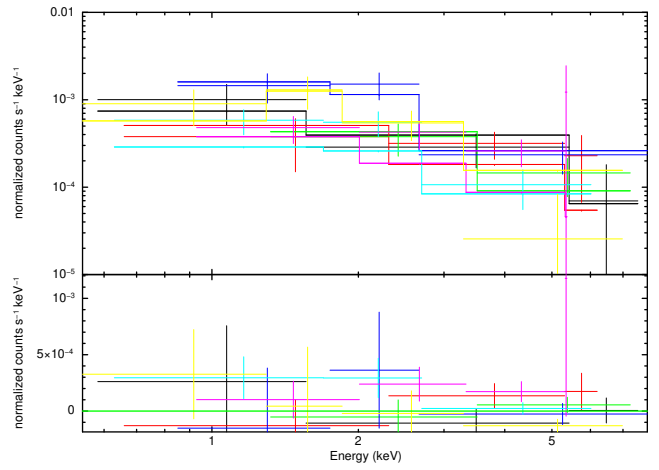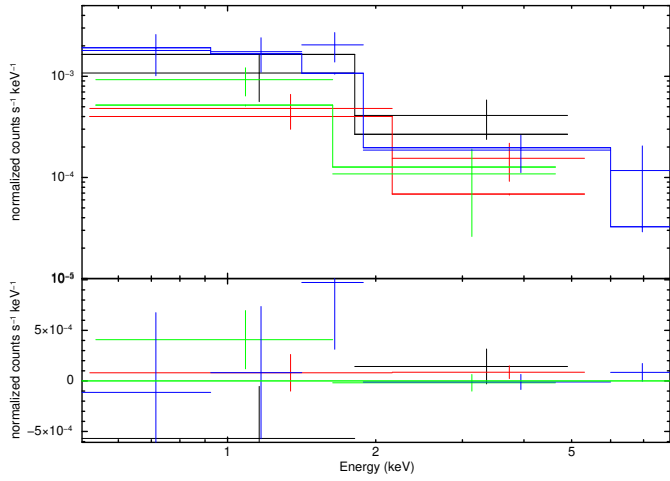
Fig. A.35. J020529.5−051100 (2,2), $z = 1.20$.

Fig. A.36. J022404.0−035730 (2,2), $z = 0.17$.
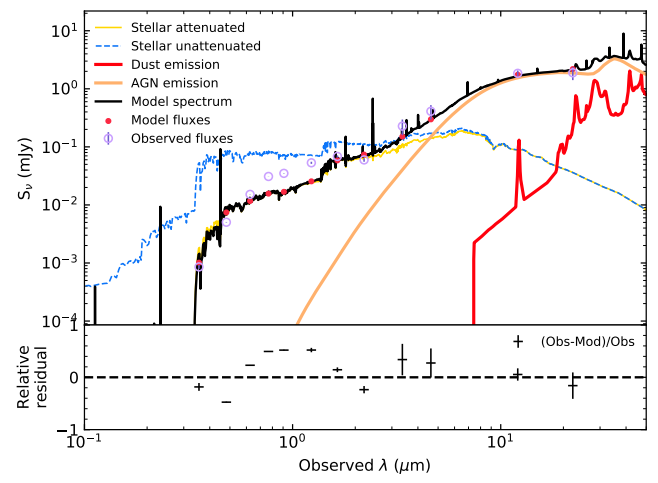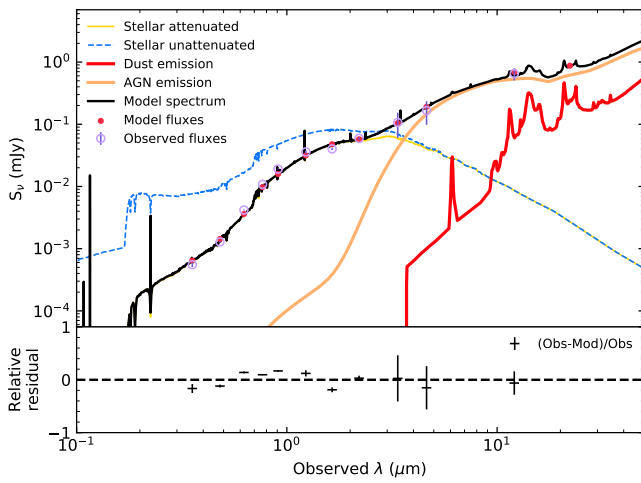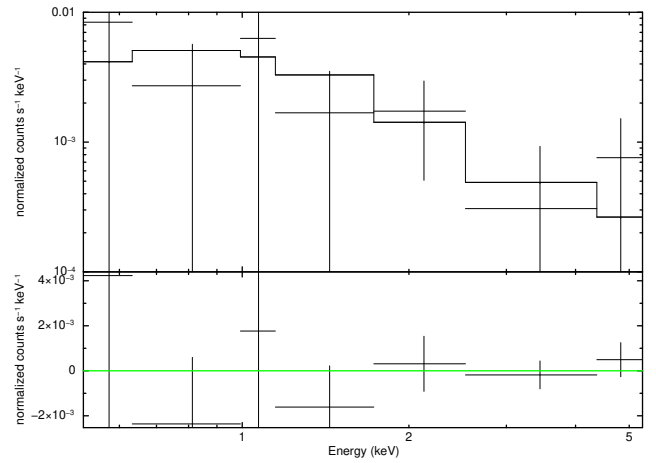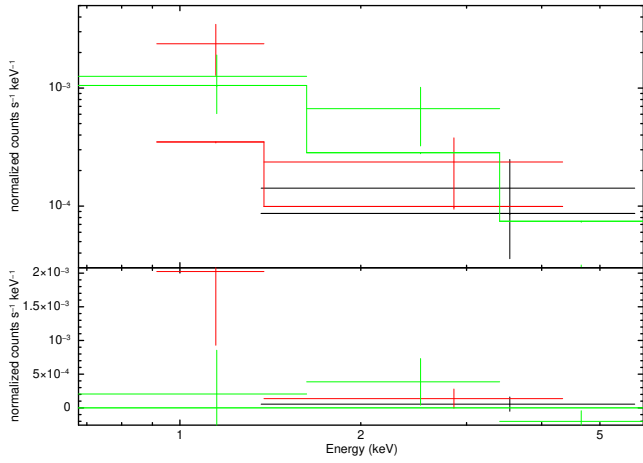
Fig. A.37. J023501.0−055234 (2,2), $z = 0.85$.

Fig. A.38. J020210.6−041129 (2,2), $z = 2.71$.
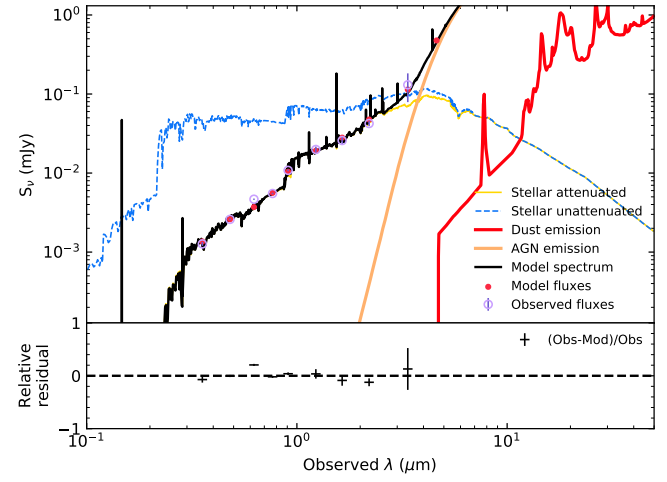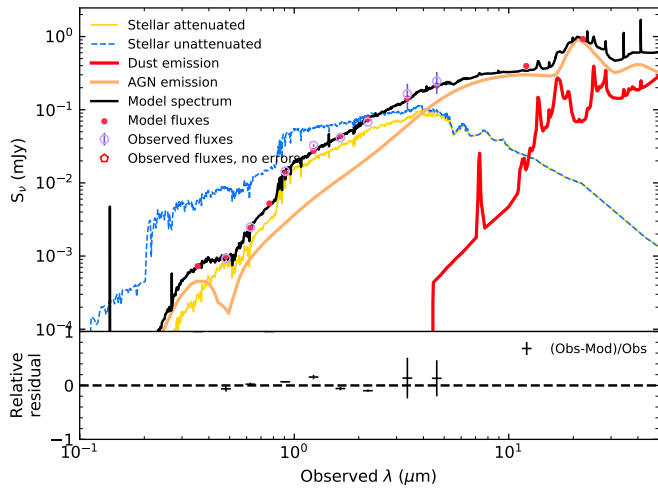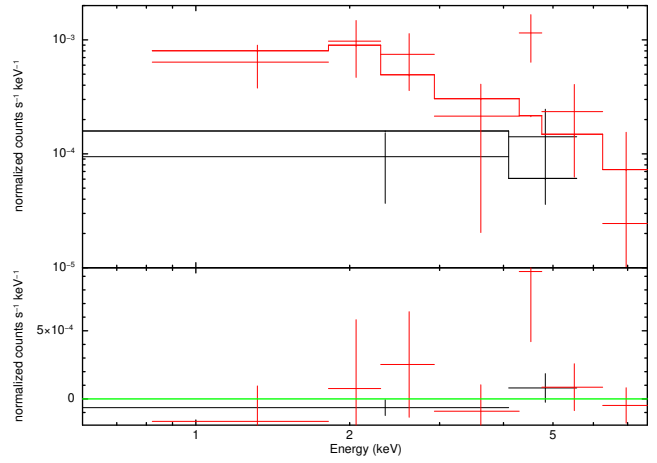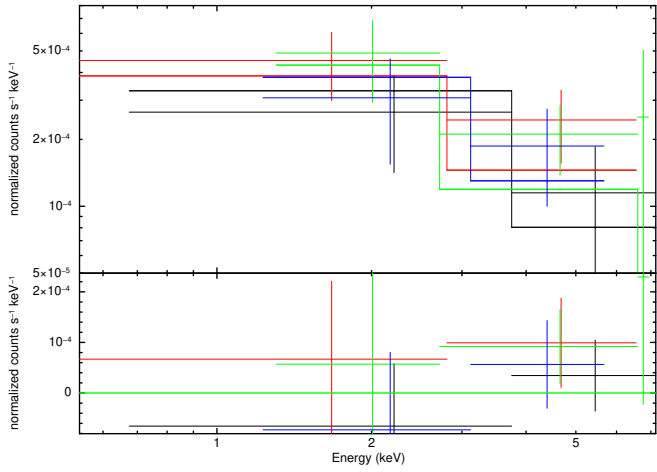
Fig. A.39. J022650.3−025752 (2,2), $z = 1.21$.

Fig. A.40. J021303.7−040704 (2,2), $z = 1.35$.
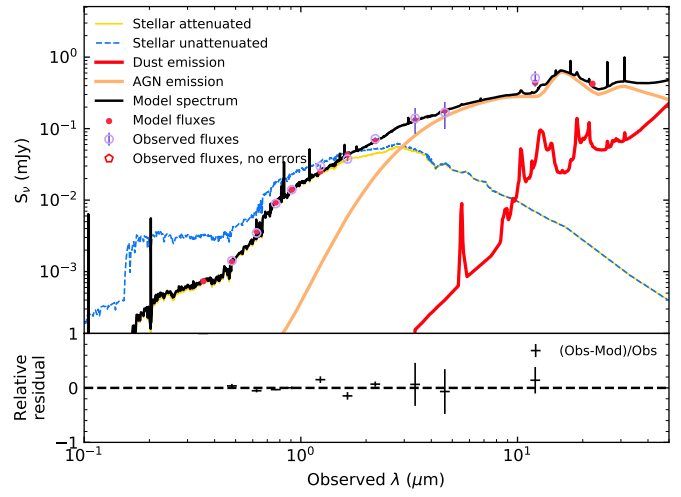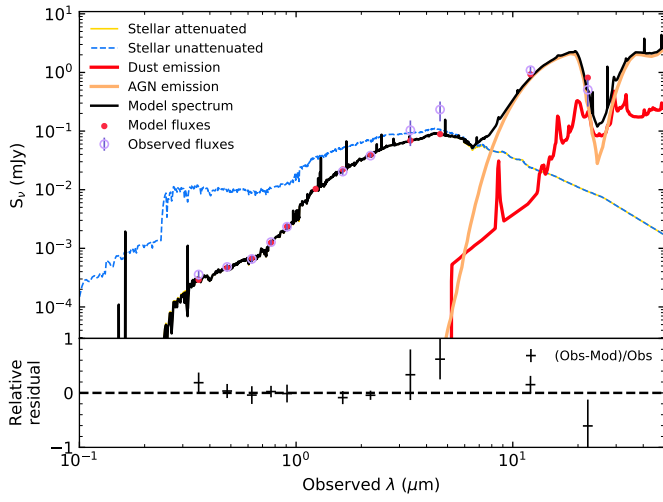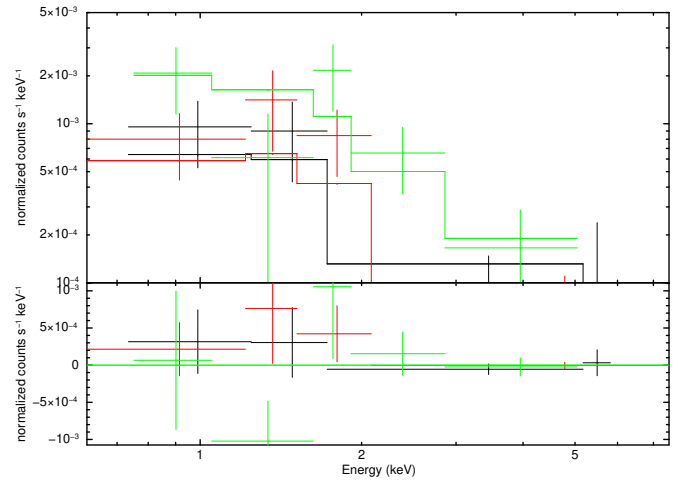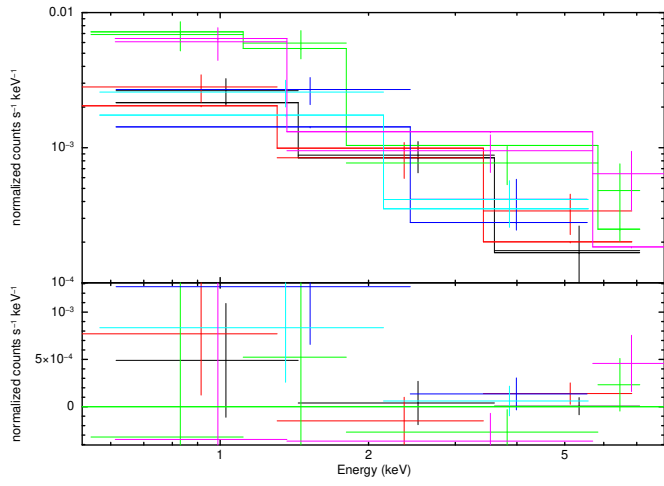
Fig. A.41. J023357.7−054819 (2,2), $z = 1.60$.

Fig. A.42. J020335.0−064450 (2,2), $z = 0.67$.
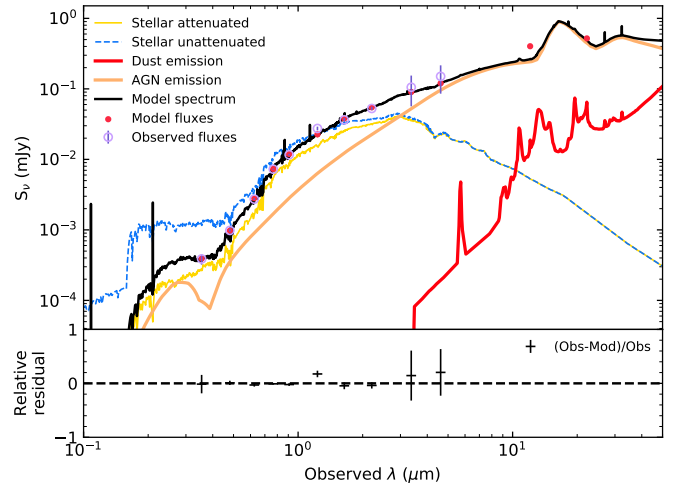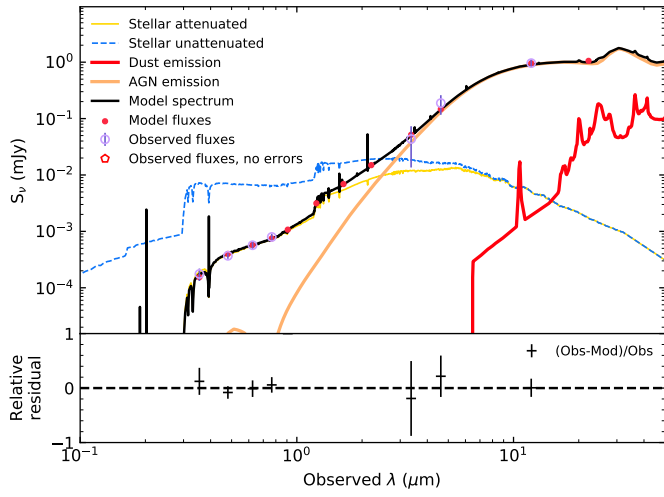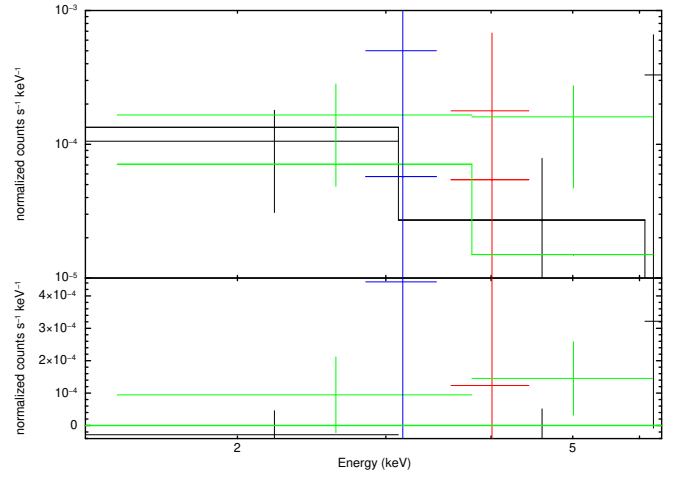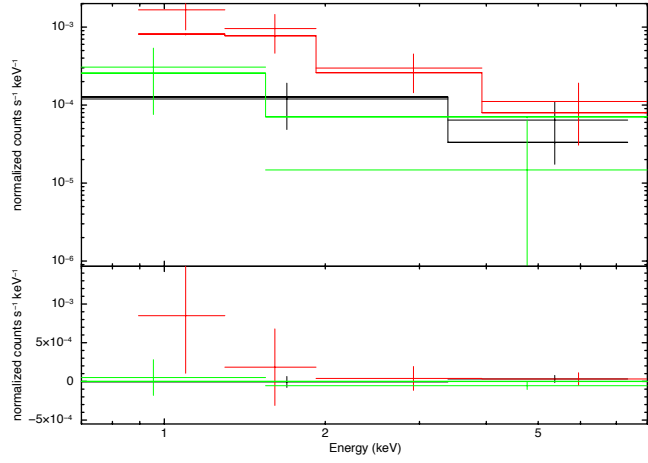
Fig. A.43. J020823.4−040652 (1,2), $z = 2.23$.

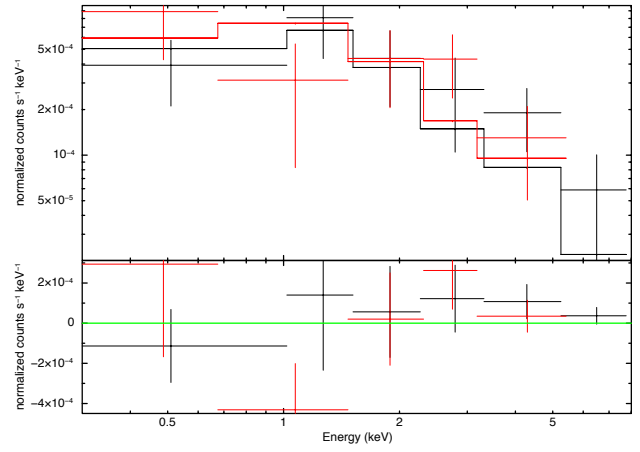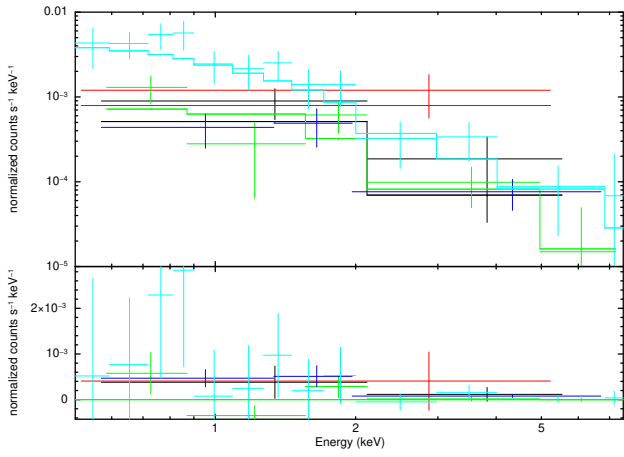**Fig. A.44.** J020135.4−050847 (1,2), $z = 0.73$.
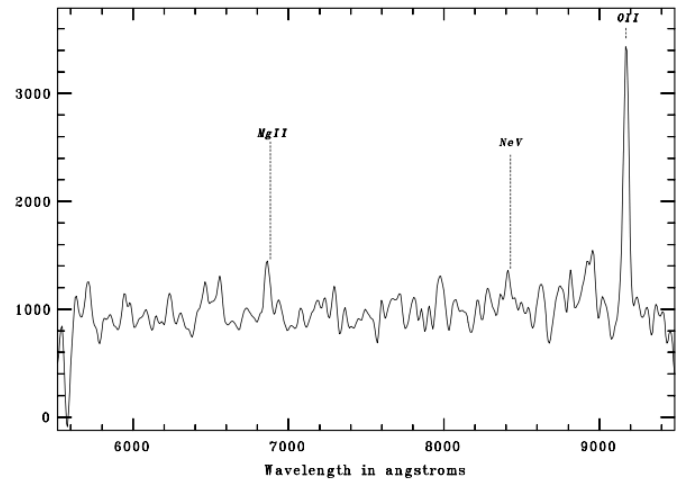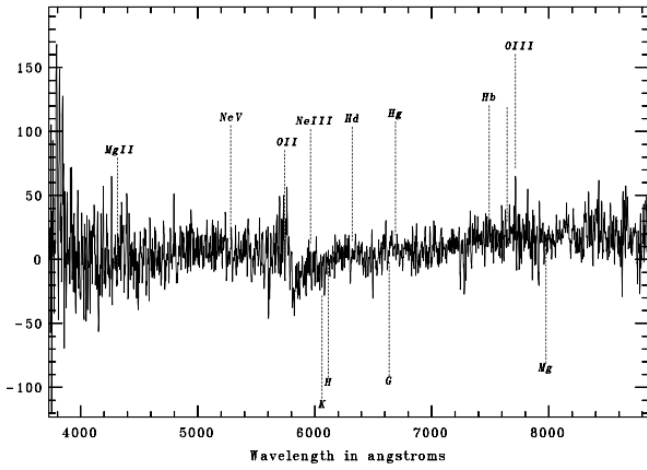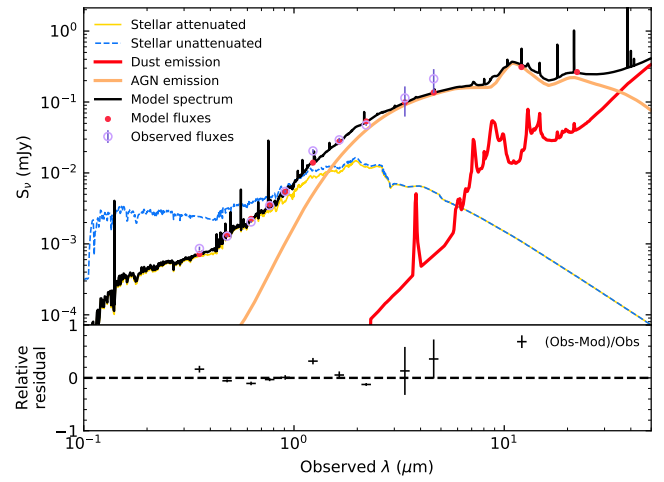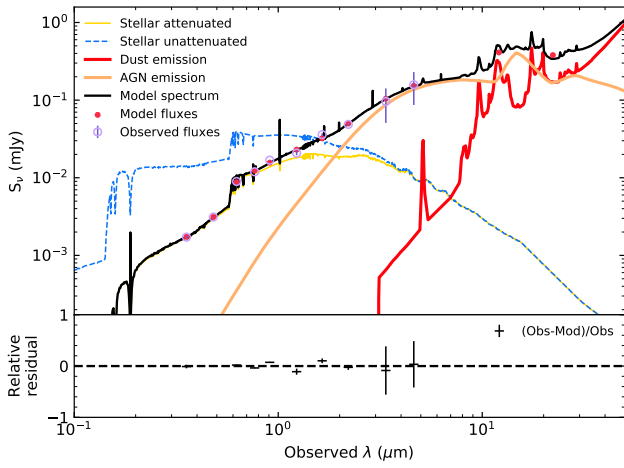
Fig. A.45. J021837.2−060654 (2,2,0), $z = 0.943$.
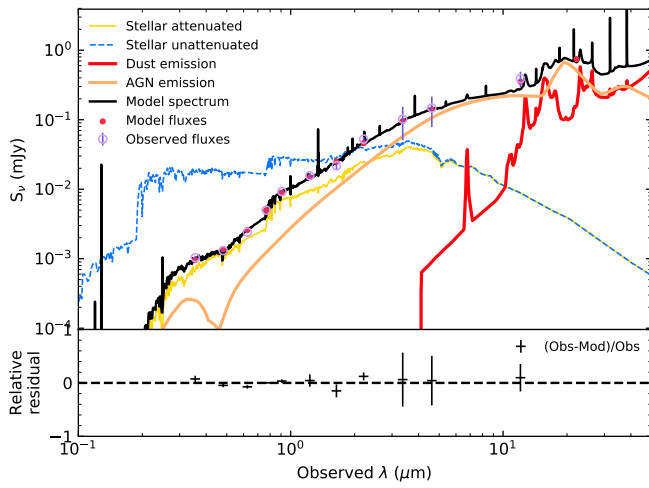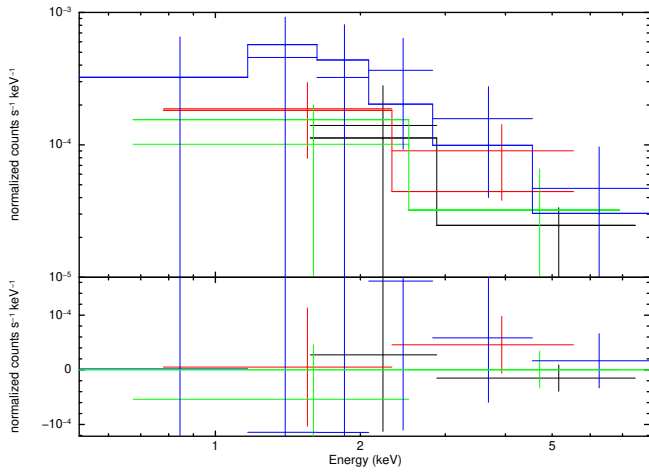

Fig. A.46. J022149.9−045920 (2,2,2), $z = 1.461$.

Fig. A.47. J020311.3−063534 (2,2), $z = 1.05$.